Journal of Nonlinear Science (2023) 33:109
https://doi.org/10.1007/s00332-023-09965-3

Journal of Nonlinear Science

Reconnection of Infinitely Thin Antiparallel Vortices and Coherent Structures

Sergei Iakunin[2] · **Luis Vega**[1,2]

Received: 2 May 2023 / Accepted: 26 August 2023 / Published online: 22 September 2023

Abstract

One of the characteristic features of turbulent flows is the emergence of many vortices which interact, deform, and intersect, generating a chaotic movement. The evolution of a pair of vortices, e.g., condensation trails of a plane, can be considered as a basic element of a turbulent flow. This simple example nevertheless demonstrates very rich behavior which still lacks a complete explanation. In particular, after the reconnection of the vortices some coherent structures with the shape of a horseshoe emerge. They have a high level of complexity generated by the interaction of waves running from the reconnection region. These structures also turn to be very reminiscent to the ones obtained from the localized induction approximation applied to a polygonal vortex. It can be considered as an evidence that a pair of vortices creates a corner singularity during the reconnection. In this work we focus on a study of the reconnection phenomena and the emerged structures. In order to do it we present a new model based on the approximation of an infinitely thin vortex, which allows us to focus on the chaotic movement of the vortex center line. The main advantage of the developed model consists in the ability to go beyond the reconnection time and to see the coherent structures. It is also possible to define the reconnection time by analyzing the fluid impulse.

Keywords Vortex reconnection · Binormal flow · Turbulence · Coherent structures · Localized induction approximation

Mathematics Subject Classification 35Q35

Communicated by Alain Goriely.

✉ Sergei Iakunin
siakunin@bcamath.org

1 University of the Basque Country (UPV/EHU), Bilbao, Spain

2 Basque Center for Applied Mathematics (BCAM), Bilbao, Spain

1 Introduction

One possible way of transition from laminar to turbulent flow is the interaction between vortices. This is a fascinating process characterized by the reconnection phenomena when the topology of vortices changes producing a cascade of smaller structures which can also reconnect. Simple examples of such processes are the interaction of a pair of vortices like a reconnection of aircraft condensation trials, considered by Crow in Crow (1970), or the collision of vortex rings (Kida et al. 1988; Lim et al. 1992). In both cases the vortices firstly undergo long-wave deformation and then reconnect generating a series of smaller rings or eye-shaped structures as those in Fig. 1. This sudden change of the flow structure is quite impressive and still not completely understood. It is also interesting that there is a surprising similarity between the statistical behavior of vortex filaments in turbulent flows for quantum and classical fluids (Bewley et al. 2008; Nemirovskii 2020). Therefore, an explanation of this phenomena may be very useful for the understanding of turbulence.

Vortices are regions in the fluid where a circular movement of particles happens. These regions can be recognized by a high magnitude of the vorticity field which is the curl of the velocity. However, the vorticity field moves with the flow, so the vortices are also moving and deforming. In non-viscous and barotropic fluid the movement of the vortex lines obeys the Navier-Stokes equations as if they were objects embedded into the flow (McGavin and Pontin 2018; Kida and Takaoka 1991). The fact that the vortices are part of a flow and also moved by it leads to that the detection and extraction of vortices from the solutions of the Navier–Stokes equations is quite challenging, and it is even more complicated to follow their evolution (McGavin and Pontin 2018).

We develop a new model of vortex interaction based on the approximation of infinitely thin vortex embedded into a non-viscous fluid. This model allows us to analyze the behavior of vortices before and after the reconnection moment. After the reconnection time the model predicts the emergence of structures very reminiscent to those obtained from the localized induction approximation (LIA) applied to an isolated eye-shaped vortex. The solution of LIA is related to Riemann's non-differentiable function (RNDF, see formula (43)). The ability of the developed model to pass beyond the reconnection time and see the coherent structures allows to establish a relation between a classical mathematical object such as RNDF and the turbulent flows.

In the simplest cases of the reconnection it is enough to consider a pair of vortex tubes, that is, cylindrical regions where the vorticity lines are parallel, and the vorticity magnitude is decaying far from the cylinder central line. Even in this case we have two different processes: deformation of the vortex core and deformation of the central line. The first one leads to the creation of the helical Kelvin waves seen in many experiments (Leweke et al. 2016), numerical simulations (Laporte and Leweke 2002), and described in detail in Le Dizés and Lacaze (2005). The presence of the Kelvin waves leads to a less clean reconnection process what makes more challenging to understand the phenomena. Their amplitude, however, depends on the size of the vortex core, so in this article we focus on infinitely thin vortices in order to avoid these waves. We will refer to this approximation as the vortex filament approximation. In our model the asymmetric helical structures of Kelvin waves before the reconnection disappear, but the symmetric ones persist. It can be considered as an indicator that

these waves have different nature: the ones before are due to the deformation of the core, but the ones after are due to the emerged singularity.

Many attempts to describe the vortex reconnection were done in the last 50 years. It started with the pioneer paper of Crow (1970) where the evolution of aircraft condensation trails is studied. A pair of initially straight vortices undergoes slow, nearly planar sinusoidal instability. However, the planes containing the deformed vortices are different and incline one to another by approximately $\pi/4$. The amplitude of the deformation grows, and after some time, the vortices reconnect forming a train of vortex rings. The stability analysis is performed in Crow (1970) under the assumption that the vortices are infinitely thin, and the viscosity can be neglected. Suppose that $\mathbf{X}_i(s,t) \subset \mathbb{R}^3$ are curves defining central lines of both vortices. We can find the velocity $\mathbf{v}$ of the flow in any point $\mathbf{x}$ outside the vortices using the Biot–Savart integral:

$$\mathbf{v}(\mathbf{x}) = \sum_{j=1}^{2} \frac{\Gamma_j}{4\pi} \int_{-\infty}^{\infty} \frac{(\mathbf{x} - \mathbf{X}_j(s,t)) \wedge \frac{\partial}{\partial s}\mathbf{X}_j(s,t) ds}{|\mathbf{x} - \mathbf{X}_j(s,t)|^3}. \tag{1}$$

Here t is time, s is the parameter of the curve, $i \in \{1,2\}$, Γ_i is the vortex strength, the symbol $\wedge$ defines the vector product, the domain is supposed to be $\mathbb{R}^3$, and the vortices are infinite. Integrals (1) after the introduction of a cutoff can be also applied to a point on the vortex providing the velocity $\frac{\partial}{\partial t}\mathbf{X}_i(s,t)$. In Crow (1970) a linear perturbation analysis is applied to a pair of initially antiparallel vortices finding that the most unstable mode is the long symmetric wave, called Crow wave. There are also short and asymmetric waves seen in experiments and predicted by the model, but their growing rate is much slower, and they probably emerge only under certain atmospheric conditions. The wavelength predicted by the Crow model for aircraft condensation trails equals $8.6b$ where b is the initial distance between vortices (aircraft wingspan). This result slightly exceeds the wavelength obtained in experiments (Ortega et al. 2003) and numerical simulations (Han et al. 2000). It happens because the finite size core enhances the growth of shorter waves, especially in the case of intense turbulence.

Even though the Crow model predicts instability, it is hard to use it for the numerical simulation or any further analysis. A series of simpler models was proposed in several papers by Klein and Majda (1991), Klein et al. (1995). Since there is only long-wave deformation, we can choose an orthonormal basis $\mathbf{e}_1$, $\mathbf{e}_2$, $\mathbf{e}_3$ and suppose that the vortices are nearly parallel to $\mathbf{e}_3$:

$$\mathbf{X}_i(s,t) = s\mathbf{e}_3 + \delta^2 \mathbf{X}_i^{(2)}\left(\frac{s}{\delta}, \frac{t}{\delta^2}\right) + o(\delta^2), \tag{2}$$

where $\delta \ll 1$, and $\mathbf{X}_i^{(2)}(s,t)$ is always orthogonal to $\mathbf{e}_3$, so it can be considered as a 2D vector. The allowed wavelength is proportional to δ, but they are still long comparing to the initial distance between vortices that is proportional to δ^2. Under this assumption

the Biot–Savart integral can be approximated up to the leading order in δ:

$$\frac{\partial}{\partial t}\mathbf{X}_i(s,t) = \mathbf{J}\left(\alpha_i\Gamma_i\frac{\partial^2}{\partial s^2}\mathbf{X}_i(s,t) + \sum_{i\neq j} 2\Gamma_j\frac{\mathbf{X}_i(s,t)-\mathbf{X}_j(s,t)}{|\mathbf{X}_i(s,t)-\mathbf{X}_j(s,t)|^2}\right), \tag{3}$$

where α_i is a constant which depends on vortex core, Γ_i is the vortex strength, and

$$\mathbf{J} = \begin{pmatrix} 0 & -1 \\ 1 & 0 \end{pmatrix}.$$

There are two terms in (3): the first one is the local self-induction that is the velocity of the flow generated by the vortex itself, whereas the second one is the velocity produced by the external flow generated by other vortices. The reconnection after finite time for this model is proven in Banica et al. (2017). Equation (3) is much easier to use for numerical simulation. However, due to the singularity in the second term it is impossible to go beyond the reconnection time. Furthermore, it is not clear whether assumption (2) holds true when the amplitude of Crow waves is large and consequently the distance between vortices is small.

Another possible approach to study the reconnection phenomena is to consider the Navier–Stokes equations. In this case we do not have any problems related to the singularity and can include all the details such as compressibility, viscosity and core deformation. The simulation, however, requires more computations and is more difficult. The direct numerical simulation (DNS) of the incompressible Navier–Stokes equations is done in Hussain and Duraisamy (2011). The visualization of vortices with the λ_2 criterion (Jeong and Hussian 1995) shows the flattering of the vortex core near the reconnection region and the formation of threads between vortex rings. These threads are stretching and may reconnect again if the Reynolds number is big enough. The presence of viscosity makes it difficult to follow vortex lines due to the dissipation. Therefore, the topology of the vortices is defined by surfaces not by the curves and is much more complicated to analyze. In McGavin and Pontin (2018) the vortex lines are extracted from the solution of the Navier–Stokes equations and classificated into ones that reconnect, threads and the additional vortex rings which emerges in the reconnection zone. It again demonstrates that these phenomena contain a lot of different effects. Another attempt is done in Yao and Hussain (2020) where the reconnection processes are divided into 3 stages: (1) the vortex cores flattering and stretching in the reconnection region; (2) cutting and reconnection of the inner vortex lines that leads to formation of bridges; (3) formation of threads from the rest vortex lines where the energy is dissipating through a turbulent cascade. More details are given in the review article (Yao and Hussain 2022). The evolution of threads in the last stage is very complicated and chaotic for high Reynolds number, that is for thin vortices or almost non-viscous fluids. Thus, if we consider the Navier–Stokes equation for small Reynolds number, then we have to deal with the deformation of the core and the dissipation due to viscosity which does not allow us to extract main coherent structures. On the other hand for high Reynolds number we face the chaotic behavior of the threads after reconnection which is also difficult to filter. We can also

note that the coherent structures emerge not only in the reconnection region but also far from it as a result of the interaction of running waves. These structures are clearer, have a distinctive horseshoe shape, and they are the focus of our attention. In particular, we highlight in this paper that they have a behavior very reminiscent to the evolution of the corner vortex under LIA.

We show in Fig. 1 the main features that emerge due to the reconnection process. We perform the solution of the Navier–Stokes equations using the large eddy simulation (LES) in OpenFOAM software. In Fig. 1a the symmetric large length Crow waves emerge. Further, in Fig. 1b we can notice small length asymmetric Kelvin waves in the region close to the reconnection. And finally after the reconnection we can see in Fig. 1c one horseshoe structure in black rectangle and the bridge going to another symmetric one. In Hussain and Duraisamy (2011), Yao and Hussain (2020, 2022), Brenner et al. (2016) the bridge is called thread, whereas the horseshoes are called bridges, but in this article we will follow the introduced terminology. In this paper we are not interested in the vortex reconnection cascade (Melander and Hussain 1988) but in the evolution of the horseshoe structures and in the complexity of the interaction of the waves that emerge. The extraction of these structures and the definition of the reconnection time are quite challenging due to the finite thickness of the vortices in the Navier–Stokes simulation.

The reconnection of vortices also happens in superfluids (Bewley et al. 2008; Fonda et al. 2019). Even though there are many differences between classical fluids and superfluids, some features of the turbulent regime have similarities, e.g., classical turbulence flows have a filamentary structure (Nemirovskii 2020). Therefore, the results in superfluid reconnection are also important for us. Instead of classical vortices, in superfluids there are quantum vortices that are topological defects where the density tends to zero. Usually the quantum vortices are studied using Gross–Pitaevskii equations (Villois et al. 2017) or doing vortex filament approximation (Schwarz 1985) since the quantum vortices are infinitely thin. There is still a problem on how to model the reconnection and the change of the topology of the vortices. In Schwarz (1985) it is done by a heuristic way of measuring the distance between nodes in the discretization of the filaments. The resulting shape demonstrates a self-similar behavior with a circular horseshoe and helical waves running along the reconnected vortices.

The configuration with the horseshoe and helical waves is very reminiscent to the evolution of a vortex filament that moves according to LIA and at the initial time is given by two half-lines that meet at point (the corner) with an angle θ (Gutiérrez 2003; Hoz and Vega 2018; Lipniacki 2003). We will call this vortex the corner vortex. Its evolution is depicted in Fig. 2. The curve is self-similar and has constant curvature $c(s,t) = c_0/\sqrt{2t}$ and torsion $\tau(s,t) = s/t$, where s is the arclength of the curve, t is time, c_0 and θ satisfy the relation $\sin\frac{\theta}{2} = e^{-\pi c_0^2/2}$ (see Gutiérrez 2003). It is possible to see that the corner is turned into a circular horseshoe quite similar to the one we can see in Fig. 1c. The parameter c_0 and the angle θ are estimated from the quantum vortex reconnection experiment in the superfluid helium ^4He studied in Fonda et al. (2019). The obtained data are consistent with the analytical results from Gutiérrez (2003), so one would expect the local induction approximation to work reasonably well, at least for quantum vortices. One of the goals of this work is to generalize the model by adding

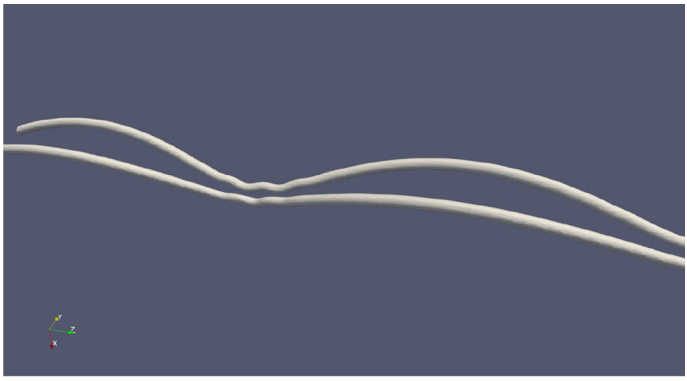

(a) Crow waves (time $t = 5$)

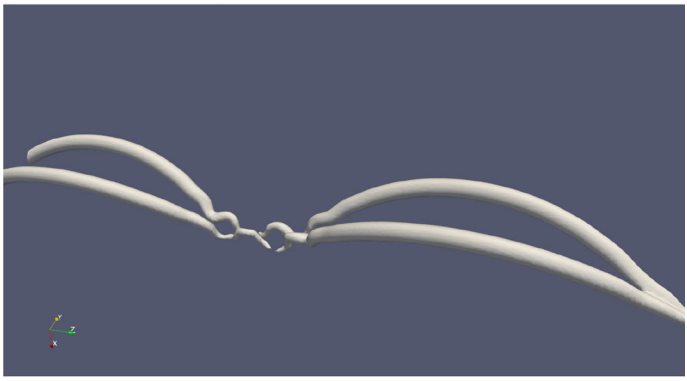

(b) Kelvin waves (time $t = 6$)

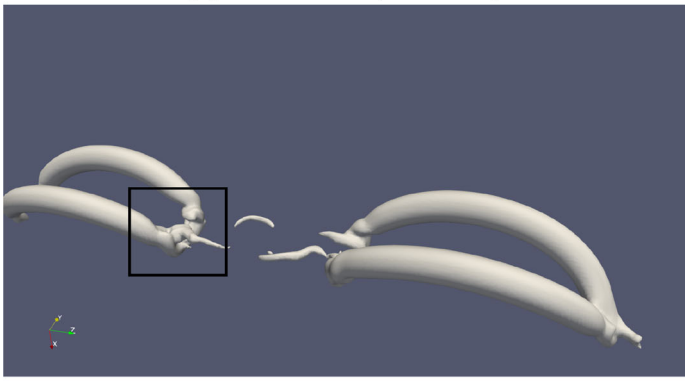

(c) Horseshoes (one in the black rectangle and the symmetric one) and bridge between them (time $t = 7$)

Fig. 1 Simulation of vortex reconnection using LES in OpenFOAM in a periodic domain of non-dimensionalized size $80 \times 80 \times 320$ discretized with $112 \times 112 \times 324$ elements. Vortex strength is $\Gamma = -1500$, vortex core radius is $r_c = 2$, and viscosity $\mu = 10^{-5}$, Re $\approx 6 \cdot 10^8$. The visualization is done with the λ_2 criterium

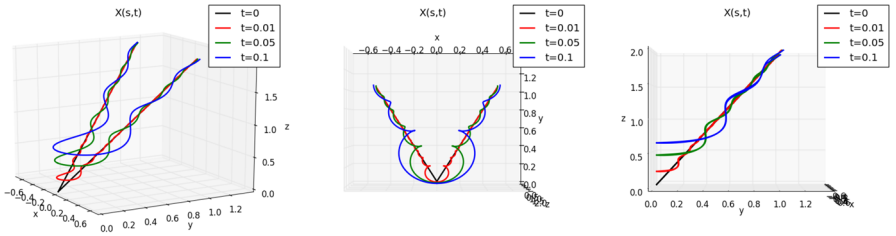

(a) 3D view (b) top view (c) side view

Fig. 2 Self-similar evolution of a corner vortex from different points of view

the interaction term and to establish a relation between the self-similar behavior of an infinitely thin corner vortex and the reconnection of vortices.

In this article we present a new model based on the vortex filament approximation but with the interaction term similar to the one in Klein et al. (1995). This model is able to go beyond the reconnection moment in a natural way, without any heuristic, and generate coherent structures. It seems to behave as the one showed in Fig. 2 that we have just explained. The reconnection time cannot be found from the configuration of vortices, so we cannot change the topology without introducing an error. However, if we focus on an integral quantity the reconnection time becomes much more clear. We study the fluid impulse that is an integral of a cross-product of position and vorticity calculated around the reconnection region. Initially this integral changes monotonically but at some time starts to oscillate. We consider this time as the reconnection time. Furthermore, the behavior of the fluid impulse after reconnection is very reminiscent to the RNDF. A similar effect for a polygonal vortex was discussed in Hoz and Vega (2018), and we can consider this as an evidence that the vortices at the reconnection seem to create a corner similar to the one described in Gutiérrez (2003).

The paper has the following structure. In Sect. 2 the derivation of the equations from the Biot–Savart law is shown. Next, in Sect. 3 we discuss some properties of the new model and its relation to the previous ones. In Sect. 4 we describe the numerical method we use to solve the derived equations. Finally, in Sect. 5 we present results of the numerical simulation, and in Sect. 6 we compare the behavior after the reconnection with the one of an isolated vortex which has the shape of an eye. It can be used as an approximation of the vortex which emerges after the reconnection (see Fig. 1c) and also as analog of a curvilinear polygon with only two corners. In Sect. 7, we make conclusions and discuss possible directions of further research. "Appendix A" is devoted to an alternative formulation and possible simplification, "Appendix B" contains the numerical algorithm, and in "Appendix C" the evolution of the eye-shaped vortex is described.

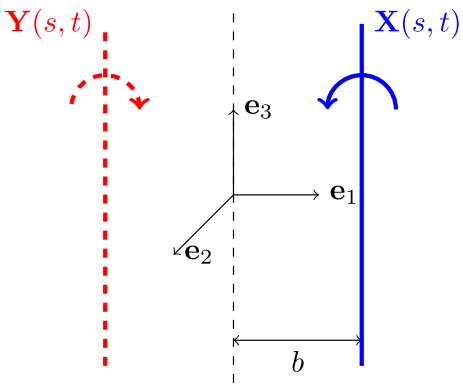

Fig. 3 Initial configuration of vortices

2 Derivation

The velocity of the flux produced by a pair of infinitely thin antiparallel vortices is given by the Biot–Savart law:

$$\mathbf{v}(\mathbf{x}) = -\frac{\Gamma}{4\pi}\left(\int_{-\infty}^{\infty} \frac{(\mathbf{x}-\mathbf{X}(s)) \wedge \frac{\partial \mathbf{X}}{\partial s}(s)}{|\mathbf{x}-\mathbf{X}(s)|^3} ds - \int_{-\infty}^{\infty} \frac{(\mathbf{x}-\mathbf{Y}(s)) \wedge \frac{\partial \mathbf{Y}}{\partial s}(s)}{|\mathbf{x}-\mathbf{Y}(s)|^3} ds\right), \tag{4}$$

where Γ is the circulation, $\mathbf{X}(s)$ and $\mathbf{Y}(s)$ are curves in $\mathbb{R}^3$ defining central lines of both vortices, the symbol $\wedge$ defines the vector product.

The vortices are moving by the flow generated by them; therefore, $\mathbf{X}(s,t)$ and $\mathbf{Y}(s,t)$ are also functions of time. For a point $\mathbf{x}$ belonging to the vortex $\mathbf{X}(s,t)$ the first integral represents the velocity due to the local self-induction $\mathbf{v}_{lia}$, and the second integral is the velocity of the external flow $\mathbf{v}_{ext}$ produced by the vortex $\mathbf{Y}(s,t)$. Then, we can decompose the velocity of the vortex filament into a sum:

$$\frac{\partial}{\partial t}\mathbf{X}(s,t) = \mathbf{v}_{lia}(s,t) + \mathbf{v}_{ext}(s,t).$$

Let us call the components of vector $\mathbf{X}(s,t) = \left(x_1(s,t)\ x_2(s,t)\ x_3(s,t)\right)^T$. The initial configuration of the vortices is depicted in Fig. 3. Now we make the following assumptions:

1. The vortices are symmetric respect to the plane $x_1 = 0$; hence, we can reduce our problem to only one unknown curve $\mathbf{X}(s,t)$ obtaining the second one by:

$$\mathbf{Y}(s,t) = \left(-x_1(s,t)\ x_2(s,t)\ x_3(s,t)\right)^T. \tag{5}$$

2. For the velocity of the external flow we will use Rosenhead regularization (Rosenhead 1930):

$$\mathbf{v}_{ext}(s,t) = \frac{\Gamma}{4\pi}\int_{-\infty}^{\infty} \frac{(\mathbf{X}(s,t)-\mathbf{Y}(q,t)) \wedge \frac{\partial \mathbf{Y}}{\partial q}(q,t)}{\left(4r_c^2 + |\mathbf{X}(s,t)-\mathbf{Y}(q,t)|^2\right)^{\frac{3}{2}}} dq, \tag{6}$$

where r_c is a parameter related to the vortex core, s is the parameter of the curve, and q is the parameter of the curve used inside the integral. This regularization prevents the singularity in the interaction term and can be understood as a viscosity effect during the merging of the cores of the vortices. For the self-induction part we do not use the regularization because there is no core merging.
3. The second vortex can be linearized near any point s that is in the interval $q \in (s - \alpha\sqrt{x_1^2(s,t) + r_c^2}, s + \alpha\sqrt{x_1^2(s,t) + r_c^2})$ for some parameter α; furthermore, the tails can be neglected in the Biot–Savart law. The length of this interval is almost proportional to the distance between vortices. When the second vortex is far, a large part of it makes a relevant contribution. On the other hand, when it is close the situation is similar to LIA because the second integral in (4) is close to singular; thus, we can consider only a small leading piece of it.
4. Either $x_1(s,t)$ or $\frac{\partial x_1(s,t)}{\partial s}$ is small, so the product $x_1(s,t)\frac{\partial x_1(s,t)}{\partial s}$ is neglectable. It means that a piece of vortex can be oriented in $\mathbf{e}_1$ direction only when it is close to the second vortex.

Self-induction Let us start from the first term in (4) which corresponds to the self-induction. Here we follow the standard derivation of the vortex filament equation for binormal flow (Shaffman 1992) using LIA. Fix a time moment and select a point $\mathbf{X}(s)$. We choose a perturbation $\rho\boldsymbol{\xi}(s) = \rho\,(\mathbf{N}(s)\cos(\theta) + \mathbf{B}(s)\sin(\theta))$ with small ρ, normal $\mathbf{N}(s)$, binormal $\mathbf{B}(s)$, and some angle θ. The self-induced velocity of the vortex is found as the limit of Biot–Savart integral when ρ goes to zero. Since the expression in the integral becomes singular, we can estimate it using only a neighborhood of the point s with a cut-off L_{lia} where we can expand $\mathbf{X}(q)$ in the Taylor series up to the third order of $|q - s|$:

$$\begin{aligned}\mathbf{v}_{lia}(s) &\approx -\frac{\Gamma}{4\pi}\int_{s-L_{lia}}^{s+L_{lia}} \frac{(\mathbf{X}(s)+\rho\boldsymbol{\xi}(s)-\mathbf{X}(q)) \wedge \mathbf{X}_q(q)}{|\mathbf{X}(s)+\delta\mathbf{X}(s)-\mathbf{X}(q)|^3} dq \\ &\approx -\frac{\Gamma}{4\pi}\int_{s-L_{lia}}^{s+L_{lia}} \Bigg(\frac{\rho\boldsymbol{\xi}(s) \wedge \left(\mathbf{X}_s(s)+(q-s)\mathbf{X}_{ss}(s)\right)}{\left(\rho^2+(q-s)^2|\mathbf{X}_s(s)|^2\right)^{\frac{3}{2}}} \\ &\qquad - \frac{(q-s)^2\mathbf{X}_s(s) \wedge \mathbf{X}_{ss}(s)}{2\left(\rho^2+(q-s)^2|\mathbf{X}_s(s)|^2\right)^{\frac{3}{2}}} \Bigg) dq,\end{aligned} \tag{7}$$

subindices here designate corresponding derivatives. We have also used that $|\boldsymbol{\xi}(s)| = 1$ and that it is orthogonal to $\mathbf{X}_s(s)$. The first term in (7) represents rotation around the vortex central line without its alteration, whereas the second one is the movement of

the central line that gives the self-induced velocity:

$$\mathbf{v}_{lia} \approx \frac{\Gamma}{4\pi}\frac{\mathbf{X}_s \wedge \mathbf{X}_{ss}}{2|\mathbf{X}_s|^3}\left(-\frac{2|\mathbf{X}_s|}{\sqrt{|\mathbf{X}_s|^2+4\frac{\rho^2}{L_{lia}^2}}}+\ln\left(\frac{\sqrt{|\mathbf{X}_s|^2+4\frac{\rho^2}{L_{lia}^2}}+|\mathbf{X}_s|}{\sqrt{|\mathbf{X}_s|^2+4\frac{\rho^2}{L_{lia}^2}}-|\mathbf{X}_s|}\right)\right).$$

In the limit $\rho/L_{lia} \to 0$ we obtain the local induction approximation (or the binormal flow):

$$\mathbf{v}_{lia}(s) = \frac{\Gamma}{4\pi}\left(-1+\ln\left(\frac{L_{lia}}{\rho}|\mathbf{X}_s(s)|\right)\right)\frac{\mathbf{X}_s(s)\wedge\mathbf{X}_{ss}(s)}{|\mathbf{X}_s(s)|^3}. \tag{8}$$

Assume that the cut-off is inverse to the modulus of tangential vector, that is $L_{lia} = \tilde{L}_{lia}/|\mathbf{X}_s(s)|$, and introduce the first parameter of our model:

$$\varepsilon = \frac{2}{-1+\ln\left(\tilde{L}_{lia}/\rho\right)}. \tag{9}$$

We will see later that the modulus of the tangential vector is growing when the time is close to the reconnection moment. However, due to the regularization in the interaction term we can bound it from above with a power of r_c. The parameter ε represents the strength of the interaction between vortices.

External flow The second integral in (4) after applying symmetry assumption, Rosenhead regularization (6) and fixing the time reads

$$\mathbf{v}_{ext}(s) = \frac{\Gamma}{4\pi}\int_{-\infty}^{\infty}\frac{(2x_1(s)\mathbf{e}_1+\mathbf{Y}(s)-\mathbf{Y}(q))\wedge\mathbf{Y}_q(q)}{\left(4r_c^2+4x_1^2(s)+4x_1(s)(y_1(s)-y_1(q))+|\mathbf{Y}(s)-\mathbf{Y}(q)|^2\right)^{\frac{3}{2}}}dq. \tag{10}$$

where component $y_1(s)$ of vector $\mathbf{Y}(s)$ is given by (5). We can apply assumption 3 obtaining:

$$\mathbf{v}_{ext}(s) \approx \frac{\Gamma}{32\pi\left(x_1^2(s)+r_c^2\right)^{3/2}}\int_{s-\alpha\sqrt{x_1^2(s)+r_c^2}}^{s+\alpha\sqrt{x_1^2(s)+r_c^2}}\frac{2x_1(s)\mathbf{e}_1\wedge\mathbf{Y}_s(s)dq}{\left(1-\frac{(q-s)x_1(s)x_{1,s}(s)-(q-s)^2|\mathbf{Y}_s(s)|^2}{x_1^2(s)+r_c^2}\right)^{3/2}}.$$

Neglecting the term $x_1(s)x_{1,s}(s)$ due to assumption 4 we obtain that the external velocity is

$$\mathbf{v}_{ext}(s) = \frac{\Gamma x_1(s)\mathbf{e}_1\wedge\mathbf{Y}_s(s)}{16\pi\left(x_1^2(s)+r_c^2\right)|\mathbf{Y}_s(s)|}\frac{2\alpha|\mathbf{Y}_s(s)|}{\sqrt{1+\alpha^2|\mathbf{Y}_s(s)|^2}} \approx \frac{\Gamma x_1(s)\mathbf{e}_1\wedge\mathbf{Y}_s(s)}{8\pi\left(x_1^2(s)+r_c^2\right)|\mathbf{Y}_s(s)|}, \tag{11}$$

if we choose α large enough.

Main equations Summing up (8) with (11) and rescaling the time with $[t] = 8\pi\varepsilon/\Gamma$ we obtain the main equations describing the evolution of a pair of symmetric vortices due to self-induction and interaction:

$$\mathbf{X}_t = \frac{\mathbf{X}_s \wedge \mathbf{X}_{ss}}{|\mathbf{X}_s|^3} - \frac{\varepsilon x_1}{x_1^2 + r_c^2} \frac{\mathbf{X}_s \wedge \mathbf{e}_1}{|\mathbf{X}_s|}. \tag{12}$$

In (12) we have also used that $|\mathbf{X}_s| = |\mathbf{Y}_s|$ and $\mathbf{X}_s \wedge \mathbf{e}_1 = \mathbf{Y}_s \wedge \mathbf{e}_1$. The equations should be equipped with an initial condition $\mathbf{X}_0(s) = \mathbf{X}(s, 0)$ which is usually a small perturbation of a line $b\mathbf{e}_1 + s\mathbf{e}_3$ shifted from the origin by a positive value b in $\mathbf{e}_1$ direction and oriented in $\mathbf{e}_3$, and the boundary conditions which we will suppose periodic on an interval $s \in (0, S)$.

The parameter ε represents the strength of the vortex interaction when compared with the self-induction. The bigger it is, the faster the reconnection happens. A more detailed relation between ε and the velocity of the vortices is shown in Sect. 3. In that section we also show how ε influences on the vortex stretching. The parameter r_c is necessary in order to avoid the singularity in the interaction term when $x_1 = 0$. However, it has a physical meaning of viscosity. According to Shaffman (1992) the radius of the vortex core $r_c \sim \sqrt{\nu t}$, where ν is viscosity and t is time. Since we are mainly interested in non-viscous reconnection the parameter r_c should be as small as possible. Even though the presence of r_c does not allow to see a sharp corner, we still can see the effect and complexity of wave interaction at later times.

3 Some Properties of the Derived Equations

Relation to previous models

The Klein–Majda system of equations (Klein et al. 1995) for a pair of nearly parallel counter-rotating vortices in the symmetric case can be obtained from Eq. (12). Indeed, in the considered case, taking into account that the vortices are nearly parallel to $\mathbf{e}_3$ and including regularization, the Klein–Majda system reads:

$$\begin{aligned} \frac{\partial \mathbf{X}}{\partial t} &= \frac{\Gamma}{4\pi}\mathbf{e}_3 \wedge \left(\sigma \frac{\partial^2 \mathbf{X}}{\partial s^2} - \frac{\mathbf{X} - \mathbf{Y}}{|\mathbf{X} - \mathbf{Y}|^2 + r_c^2} \right), \\ \frac{\partial \mathbf{Y}}{\partial t} &= -\frac{\Gamma}{4\pi}\mathbf{e}_3 \wedge \left(\sigma \frac{\partial^2 \mathbf{Y}}{\partial s^2} - \frac{\mathbf{Y} - \mathbf{X}}{|\mathbf{Y} - \mathbf{X}|^2 + r_c^2} \right). \end{aligned} \tag{13}$$

Parameter σ here depends on the structure of the vortex core, $\mathbf{X}$ and $\mathbf{Y}$ here are 2-dimensional vectors, the third component $x_3(s, t) = y_3(s, t) = s$ is known and ignored in the system. We can reduce the number of equations using symmetry:

$$x_{1,\tilde{t}} = -x_{2,ss}, \quad x_{2,\tilde{t}} = x_{1,ss} - \varepsilon \frac{x_1}{x_1^2 + r_c^2}, \tag{14}$$

where $\tilde{t} = \frac{\Gamma}{4\pi}\sigma t$ is the rescaled time and $\varepsilon = 1/\sigma$. Now we will consider Eq. (12) supposing that the vortex central line is given in the shape

$$\mathbf{X}(s,t) = s\mathbf{e}_3 + a\mathbf{X}^{(2)}(\xi s, \tau t), \tag{15}$$

where $\mathbf{X}^{(2)} \cdot \mathbf{e}_3 = 0$ and $\xi a \ll 1$. It means that similarly to (14) we have only 2 unknowns, and that the vortices may deviate from the straight line in only a long-wave shape, comparing with the distance between vortices. In the Klein–Majda paper (Klein and Majda 1991) these waves are called short waves. However, if we compare them with the distance between vortices they are long. Plugging (15) into (12) and canceling the amplitude a we obtain:

$$\tau\mathbf{X}_t^{(2)} = \xi^2\mathbf{e}_3 \wedge \mathbf{X}_{ss}^{(2)} - \varepsilon\frac{x_1^{(2)}}{r_c^2 + x_1^2}\mathbf{e}_2 + O(a\xi).$$

We suppose that the left-hand side and the first two terms of the right-hand side are of the same order, whereas the rest is smaller; thus, multiplying by a, we get:

$$\mathbf{X}_t = \mathbf{e}_3 \wedge \mathbf{X}_{ss} - \varepsilon\frac{x_1}{r_c^2 + x_1^2}\mathbf{e}_2,$$

that is equivalent to (14).

Crow instability Linear stability analysis of (12) predicts a long-wave instability described by Crow in Crow (1970). Suppose that initially the vortices are parallel to $\mathbf{e}_3$, as depicted in Fig. 3, and add a perturbation:

$$\mathbf{X}(s,t) = b\mathbf{e}_1 + vt\mathbf{e}_2 + s\mathbf{e}_3 + \delta e^{\mu t}\begin{pmatrix}\alpha\cos\omega s\\ \beta\cos\omega s\\ \gamma\sin\omega s\end{pmatrix} + O(\delta^2), \tag{16}$$

where b is a half of the initial distance between vortices, $\delta \ll 1$. Without the perturbation the pair of vortices will move in $\mathbf{e}_2$ direction with velocity

$$v = -\varepsilon\frac{b}{b^2 + r_c^2}, \tag{17}$$

that is proportional to ε and almost inverse to the distance between vortices. This result coincides with many previous researches (Crow 1970), with experiments, and with numerical simulation using the Navier–Stokes equations. Moreover, here we get another physical meaning of the parameter ε: the bigger it is the faster the pair of vortices moves in the $\mathbf{e}_2$ direction.

Now let us find the frequencies of perturbations for which this straight line solution is not stable. Plugging (16) into (12) and keeping only linear terms respect to δ we

obtain

$$\mu \begin{pmatrix} \alpha \cos \omega s \\ \beta \cos \omega s \\ \gamma \sin \omega s \end{pmatrix} = -\omega^2 \begin{pmatrix} -\beta \cos \omega s \\ \alpha \cos \omega s \\ 0 \end{pmatrix} - \varepsilon \alpha \mathbf{e}_2 \frac{r_c^2 - b^2}{\left(b^2 + r_c^2\right)^2} \cos \omega s - \frac{\varepsilon \beta \mathbf{e}_3 b}{b^2 + r_c^2} \sin \omega s.$$

We have an eigenvalue problem

$$\mu \begin{pmatrix} \alpha \\ \beta \\ \gamma \end{pmatrix} = \begin{pmatrix} 0 & \omega^2 & 0 \\ -\omega^2 - \varepsilon \frac{r_c^2 - b^2}{(b^2 + r_c^2)^2} & 0 & 0 \\ 0 & -\frac{\varepsilon b}{b^2 + r_c^2} & 0 \end{pmatrix} \begin{pmatrix} \alpha \\ \beta \\ \gamma \end{pmatrix}, \tag{18}$$

and perturbed solution (16) is unstable if at least one eigenvalue of (18) has positive real part. It happens for the following frequencies ω and wavelengths $\lambda = 2\pi/\omega$:

$$\omega < \frac{\sqrt{\varepsilon(b^2 - r_c^2)}}{b^2 + r_c^2}, \quad \lambda > \frac{2\pi b}{\sqrt{\varepsilon}} \left(\frac{1 + (r_c/b)^2}{\sqrt{1 - (r_c/b)^2}} \right). \tag{19}$$

Since r_c represents the radius of the vortex core and is always smaller than the initial distance between vortices, the square root in expression (19) is always real. These waves are long and called Crow waves since they were firstly described in Crow (1970).

It is important to note that since we consider Eq. (12) on the interval $s \in (0, S)$ with periodic boundary conditions we have to be sure that Crow waves (19) fit in this interval, that is $S \geq \lambda$. It is also interesting that velocity (17) depends on ε/b, whereas wavelength (19) depends on $\sqrt{\varepsilon}/b$; therefore, we cannot reduce number of parameters and consider only the ratio. Further we will see that ε affects not only on the speed of the reconnection but also on the angle the vortices make at that moment.

The modulus of the tangential vector The vortex filament equations preserve the modulus of the tangential vector $\mathbf{T} = \mathbf{X}_s$. However, when we have the interaction term as in (12) it is not true anymore. Nevertheless, we can derive a closed expression for the modulus $|\mathbf{T}|$. In order to do it we take a derivative of (12) respect to s and calculate the inner product with $\mathbf{T}$:

$$|\mathbf{T}| \frac{\partial}{\partial t} |\mathbf{T}| = -\varepsilon \frac{x_1}{x_1^2 + r_c^2} \frac{(\mathbf{T}_s \wedge \mathbf{e}_1) \cdot \mathbf{T}}{|\mathbf{T}|} = -\varepsilon \frac{x_1}{x_1^2 + r_c^2} \frac{(\mathbf{T} \wedge \mathbf{T}_s) \cdot \mathbf{e}_1}{|\mathbf{T}|}. \tag{20}$$

We can also calculate the inner product of $\mathbf{X}_t$ with $\mathbf{e}_1$ simplifying the expression of the right-hand side of (20):

$$x_{1,t} = \frac{(\mathbf{T} \wedge \mathbf{T}_s) \cdot \mathbf{e}_1}{|\mathbf{T}|^3}. \tag{21}$$

Combining (20) with (21) and integrating respect to time we find the expression for the modulus of the tangential vector:

$$|\mathbf{T}(s,t)| = L_0(s)\left(x_1^2(s,t) + r_c^2\right)^{-\varepsilon/2}, \tag{22}$$

where $L_0(s)$ is a function which does not depend on time and is given by the initial conditions. The modulus $\mathbf{T}$ is growing in the reconnection region (that is x_1 goes to 0) and even tends to a singularity when r_c tends to 0. It can be understood as a vortex stretching phenomenon.

Self-similar solution When r_c goes to zero, Eq. (12) has self-similar solutions. Let us define $\eta = s/\sqrt{t}$ and plug $\mathbf{X}(s,t) = \sqrt{t}\mathbf{G}(\eta)$ into (12) assuming that $r_c = 0$:

$$\frac{1}{2\sqrt{t}}\mathbf{G}(\eta) - \frac{\eta}{2\sqrt{t}}\mathbf{G}'(\eta) = \frac{\mathbf{G}'(\eta)\wedge\mathbf{G}''(\eta)}{\sqrt{t}|\mathbf{G}'(\eta)|^3} - \frac{\varepsilon}{\sqrt{t}G_1(\eta)}\frac{\mathbf{G}'(\eta)\wedge\mathbf{e_1}}{|\mathbf{G}'(\eta)|}.$$

It is easy to see that after multiplying by $\sqrt{t}$ we get an ODE for $\mathbf{G}(\eta)$:

$$\frac{1}{2}\mathbf{G}(\eta) - \frac{1}{2}\eta\mathbf{G}'(\eta) = \frac{\mathbf{G}'(\eta)\wedge\mathbf{G}''(\eta)}{|\mathbf{G}'(\eta)|^3} - \frac{\varepsilon}{G_1(\eta)}\frac{\mathbf{G}'(\eta)\wedge\mathbf{e_1}}{|\mathbf{G}'(\eta)|}. \tag{23}$$

In order to extract the highest derivative we can calculate the cross-product of (23) with $\mathbf{G}'(\eta)$:

$$\frac{1}{2}\mathbf{G}\wedge\mathbf{G}' = \frac{\mathbf{G}''}{|\mathbf{G}'|} - \frac{\mathbf{G}''\cdot\mathbf{G}'}{|\mathbf{G}'|^3}\mathbf{G}' - \frac{\varepsilon|\mathbf{G}'|}{G_1}\mathbf{e}_1 + \frac{\varepsilon G_1'}{|\mathbf{G}'|G_1}\mathbf{G}'.$$

Observe that $\mathbf{G}''\cdot\mathbf{G}' = |\mathbf{G}'|\frac{d}{d\eta}|\mathbf{G}'|$, and it can be expressed by lower derivatives similarly to the previous paragraph. Thus, the final equation is:

$$\mathbf{G}'' = |\mathbf{G}'|\frac{1}{2}\mathbf{G}\wedge\mathbf{G}' + \frac{\varepsilon|\mathbf{G}'|}{G_1}\mathbf{e}_1 + \varepsilon\frac{\mathbf{G}'}{|\mathbf{G}'|}\left(\frac{1}{\eta} - 2\frac{G_1'}{G_1}\right). \tag{24}$$

Equation (24) should be equipped with two initial conditions: $\mathbf{G}(0)$ and $\mathbf{G}'(0)$. It is not clear which initial conditions we have to impose for the reconnection problem.

The self-similar solution for model (3) is studied in Banica et al. (2017). It appears that if a singularity is introduced at the beginning, it will persist for the infinite time. Thus, the self-similar reconnection in model (3) will never have a clear horseshoe in difference with the corner vortex studied in Gutiérrez (2003). One of the reasons can be that in model (3) the LIA term has a linear approximation. In Eq. (24) we include this term in the complete nonlinear form.

Behavior close to the reconnection point Using formula (22) we can bound $T_1/\|\mathbf{T}\|$ before the reconnection moment from below. Assume that in the interval $s \in [s_0, s_1]$ the component $x_1(s)$ is growing monotonically (so $T_1(s) \geq 0$) for value $m = x_1(s_0)$ to $M = x_1(s_1)$. This assumption is correct before reconnection, but the numerical

simulation shows that it does not hold true after it since the helical waves emerge. Subject to the proposed assumption we can write the following estimation:

$$\sup_{s\in(s_0,s_1)}\frac{|T_1|}{\|\mathbf{T}\|}\geq\frac{1}{s_1-s_0}\int_{s_0}^{s_1}\frac{|T_1|}{\|\mathbf{T}\|}ds=\frac{1}{s_1-s_0}\int_{s_0}^{s_1}\frac{x_1'ds}{L_0(s)\left(x_1^2+r_c^2\right)^{-\varepsilon/2}}$$
$$\geq\frac{r_c^{\varepsilon}x_1(s)}{(s_1-s_0)\|L_0\|_{C([s_1,s_0])}}{}_2F_1\left(\frac{1}{2},-\frac{\varepsilon}{2},\frac{3}{2},-\frac{x_1^2(s)}{r_c^2}\right)\Bigg|_{s_0}^{s_1},\qquad(25)$$

where $\|L_0\|_{C([s_1,s_0])}=\sup_{s\in(s_0,s_1)}|L_0(s)|$, and ${}_2F_1(a,b,c,d)$ is the hypergeometric function, the modulus of the tangential vector is given by (22). Assume now for simplicity that $r_c=0$, the reconnection happens at $s_0=0$, and designate $s_1=s$. Then, estimate (25) reads

$$\sup_{q\in(0,s)}\frac{|T_1|}{\|\mathbf{T}\|}\geq\frac{x_1^{1+\varepsilon}(s)}{s(1+\varepsilon)\|L_0\|_{C([0,s])}}.\qquad(26)$$

If initially the vortices were oriented into x_3 direction and separated by value $2b$ the norm $\|L_0\|_{C([0,s])}=b^{\varepsilon}$. The furthest point between vortices corresponds to $s=\lambda/2$, where λ is the wavelength of Crow waves given by (19). The value of $x_1(s)$ in this point is not smaller than b, so we can use it to estimate the ratio $\frac{|T_1|}{\|\mathbf{T}\|}$:

$$\sup_{q\in(0,s)}\frac{|T_1|}{\|\mathbf{T}\|}\geq\frac{\sqrt{\varepsilon}}{(1+\varepsilon)\pi}.\qquad(27)$$

This bound is not optimal and is very far from it. Nevertheless, we can expect that the first component of the tangent vector will grow when we increase ε tending it to 1. The numerical experiments in Sect. 5 show that it becomes almost parallel to $\mathbf{e_1}$, so the shape of the vortex after reconnection is very close to a horseshoe.

We can also use formula (26) to estimate the maximal possible value of x_1. Indeed, the left-hand side cannot be bigger than 1, so assuming that $\|L_0\|_{C([0,s])}=b^{\varepsilon}$ and the maximum for $x_1(s)$ is achieved at $s=\lambda/2$ we obtain;

$$x_1(s)\leq b\left(\frac{(1+\varepsilon)\pi}{\sqrt{\varepsilon}}\right)^{\frac{1}{1+\varepsilon}}.$$

4 Numerical Method

In this section we describe the numerical method we use to solve system (12). The main problem for numerical stability of the method is related to the interaction term which grows when the vortices are close to each other. We consider a simpler case of Klein–Majda equations (14) to derive possible restrictions for the numerical method. They come from the relation between the time step τ, the spatial discretization step

h and the regularization parameter r_c. Even though we use a more advanced Runge–Kutta–Fehlberg method and Eq. (12) has higher nonlinearity, the derived restrictions hold true in a qualitative way.

Necessary stability conditions We derive the necessary stability conditions for a simpler case of Klein–Majda equations (14). Consider the following semi-implicit numerical scheme:

$$x_n^{(k+1)} = x_n^{(k)} - \frac{\tau}{h^2}\left(y_{n+1}^{(k)} - 2y_n^{(k)} + y_{n-1}^{(k)}\right), \tag{28}$$

$$y_n^{(k+1)} = y_n^{(k)} + \frac{\tau}{h^2}\left(x_{n+1}^{(k+1)} - 2x_n^{(k+1)} + x_{n-1}^{(k+1)}\right) - \varepsilon\tau\frac{x_n^{(k+1)}}{{x_n^{(k+1)}}^2 + r_c^2}; \tag{29}$$

where $x_n^{(k)}$ and $y_n^{(k)}$ are approximation of first and second components, respectively, of the solution $\mathbf{X}(s_n, t_k)$; h and τ are discretization steps for the parameter s and time, respectively. Assume now that there is a high-frequency but small-amplitude numerical error $\delta^{(k)}\cos(\omega n)$ in the second component and let us analyze how it will grow on the next time step. Plugging the perturbed values $x_n^{(k)} + \delta_x^{(k)}\cos(\omega n)$ and $y_n^{(k)} + \delta_y^{(k)}\cos(\omega n)$ into (28), (29) we get for the following expression for the linear approximation of the error:

$$\delta_x^{(k+1)}\cos(\omega n) = \left(\delta_x^{(k)} + \lambda\zeta\delta_y^{(k)}\right)\cos(\omega n), \tag{30}$$

$$\delta_y^{(k+1)}\cos(\omega n) = \left(-(\lambda\zeta + \mu)\delta_x^{(k)} + (1 - \lambda^2\zeta^2 - \lambda\zeta\mu)\delta_y^{(k)}\right)\cos(\omega n), \tag{31}$$

where

$$\lambda = \tau/h^2, \quad \mu = \epsilon\tau\frac{r_c^2 - {x_n^{(k)}}^2}{\left(r_c^2 + {x_n^{(k)}}^2\right)^2}, \quad \zeta = 2(1 - \cos\omega). \tag{32}$$

The necessary stability condition requires the eigenvalues of the error transformation matrix be not bigger than 1 by modulus. From (30), (31) we obtain the equation of the eigenvalues ν:

$$\begin{vmatrix} 1-\nu & \lambda\zeta \\ -\lambda\zeta - \mu & 1 - \lambda^2\zeta^2 - \lambda\zeta\mu - \nu \end{vmatrix} = \nu^2 - (2 - \lambda^2\zeta^2 - \lambda\zeta\mu)\nu + 1 = 0.$$

The product of the eigenvalues is always 1; therefore, the necessary stability condition is satisfied if and only if the roots are complex, that is:

$$0 \le \lambda^2\zeta^2 + \lambda\zeta\mu \le 4, \tag{33}$$

implying

$$\lambda\zeta < \frac{-\mu + \sqrt{\mu^2 + 16}}{2}. \tag{34}$$

This condition can be resolved providing a constraint for τ:

$$\tau \leq \frac{2h^2}{\sqrt{\zeta^2 + \varepsilon h^2 \zeta \frac{r_c^2 - x_n^{(k)^2}}{\left(r_c^2 + x_n^{(k)^2}\right)^2}}}, \tag{35}$$

for any ω and $x_n^{(k)}$. The condition has the strongest form when ζ achieves it maximal value ($\zeta = 4$, see (32)) and $x_n^{(k)} = 0$, so the condition for τ reads:

$$\tau \leq \frac{h^2}{\sqrt{4 + \varepsilon \frac{h^2}{r_c^2}}}. \tag{36}$$

Note that for smaller r_c we have to use smaller time step. Furthermore, the stability of the scheme is lost when r_c tends to 0 what corresponds to the emergence of a singularity in the interaction term. Formula (36) implies that for say a two times smaller regularization parameter r_c we have to use a two times smaller time step τ. However, this relation does not hold true for a higher-order scheme. Indeed, in that case we will have a higher derivative of the interaction term respect to x. That is the terms h^3/r_c^3 and further will be presented in the constraint for τ. The stability can be obtained by choosing h proportional to r_c, so all terms in the Taylor expansion of the interaction term will be bounded. However, this choice leads to a very fast growth of computations, making it very hard to perform the simulation for small r_c.

Description of the numerical scheme The main challenge in the numerical solution of Eq. (12) is that at the reconnection moment the behavior of the interaction term is close to singular. This time period should be passed with very small time step which is not needed when the vortices are far from each other. Therefore, we use an adaptive time step technique: an embedded 5th Runge–Kutta method in time with 8th-order finite difference discretization in the filament parameter s. The 8th-order scheme gives the best results of those we have tried. On one hand, the spectral method that has a higher order requires a higher-order time scheme. On the other hand, a lower-order spatial discretization does not provide sufficient accuracy, and the method becomes unstable close to the reconnection point, where the solution tends to singular. We have also studied the possibility of use of implicit methods, such as Buttke (1986), but these methods suffer the same requirement of the small time step at the reconnection moment. Besides, we are interested in the multifractal behavior of the trajectories of the vortex filament points; therefore, we need data with very high discretization in time; thus, such advantage of implicit method as large time step cannot be used.

In the implementation of the method we follow the book of Butcher (2008). The idea of the embedded Runge–Kutta method consists in realization of two Runge–Kutta schemes on the same points one of order p and another one of order $p + 1$. The difference between the outputs of these methods on each step is used for the error estimation which should have the decay τ^5. If the error is bigger, then we decrease the time step until the accuracy test is passed. The explicit k-steps Runge–Kutta scheme

for an ODE $x'(t) = f(x,t)$ at step n is given by

$$q_i = f\left(t_n + \alpha_i \tau, x_n + \tau \sum_{l=1}^{i-1} \beta_{il} q_l\right), \ 1 \le i < k; \tag{37}$$

$$x_{n+1} = x_n + \tau \sum_{i=1}^{k-1} c_i q_i; \tag{38}$$

where τ is the time step; α_i, β_{il}, and c_i are the coefficients of the scheme. Usually the coefficients are given in the Butcher table: $\begin{array}{c|c} \boldsymbol{\alpha} & \boldsymbol{\beta} \\ \hline & \mathbf{c}^T \end{array}$. In order to add the accuracy test we have to add another vector of coefficients $\hat{\mathbf{c}}$ for the embedded method. We are using Runge–Kutta–Fehlberg method with the coefficients obtained in Fehlberg (1969). The adaptive time step allows to decrease the time step when it is necessary. In our case when the reconnection happens, the interaction term is very close to singular and therefore, a much smaller time step comparing with the rest of the simulation has to be used.

To make the solution more stable we use the idea of Hoz and Vega (2014) and resolve the equations for $\mathbf{X}$ and $\mathbf{T}$ at the same time adding also the arclength correction according to (22). The new equations read

$$\mathbf{X}_t = \frac{\mathbf{T}\wedge\mathbf{T}_s}{|\mathbf{T}|^3} - \frac{\varepsilon x_1}{x_1^2 + r_c^2}\frac{\mathbf{T}\wedge\mathbf{e}_1}{|\mathbf{T}|}. \tag{39}$$

$$\mathbf{T}_t = \frac{\mathbf{T}\wedge\mathbf{T}_{ss}}{|\mathbf{T}|^3} - 3\frac{\mathbf{T}\wedge\mathbf{T}_s}{|\mathbf{T}|^4}\frac{\partial|\mathbf{T}|}{\partial s} - \frac{\varepsilon}{\left(x_1^2+r_c^2\right)|\mathbf{T}|}\left(x_1\mathbf{T}_s\wedge\mathbf{e}_1 + \left(\frac{r_c^2-x_1^2}{x_1^2+r_c^2} - \frac{x_1}{|\mathbf{T}|}\frac{\partial|\mathbf{T}|}{\partial s}\right)\mathbf{T}\wedge\mathbf{e}_1\right). \tag{40}$$

Expression (22) for the modulus of the tangential vector allows us to avoid the calculation of the derivative:

$$\frac{\partial|\mathbf{T}(s,t)|}{\partial s} = \left(\frac{L_0'(s)}{L_0(s)} - \varepsilon\frac{x_1(s,t)T_1(s,t)}{x_1^2(s,t)+r_c^2}\right)|\mathbf{T}(s,t)|. \tag{41}$$

Here $L_0(s)$ and its derivative are given as initial condition. Following (Hoz and Vega 2014) we also perform the correction of the tangential vector modulus after each interaction using formula (22). The method is explained in detail in "Appendix B."

Even though there are two connected unknowns x_1 and T_1, the solution of system (39)–(40) provides the correct result $T_1 = x_{1,s}$. One can wonder whether it is possible to reduce the number of unknowns and what is the minimal number of independent functions which describe the evolution of the vortex reconnection. This is studied in "Appendix A" using the Frenet frame. It turns out that the reconnection of vortices can be described in terms of just two functions: $x_1(s,t)$ and its derivative with respect to

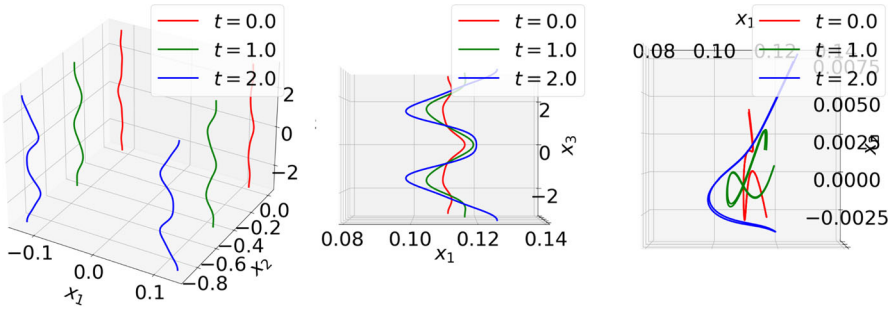

Fig. 4 Formation of Crow waves for $\varepsilon = 0.05$ and $r_c = 0.0025$. 500 nodes are used in the discretization. In the front view picture we show only right vortex; in the top view, the vortices are shifted by the mean value in x_2 direction

time $x_{1,t}(s, t)$. However, the equations in this case contain derivatives respect to s up to the 4th order. Thus, it is much more complicated for the numerical solution.

5 Results

We use the method described in Sect. 4 to solve Eq. (12). There are a few things we are mainly interested in: (1) the emergence of Crow waves and their length; (2) the influence of r_c to the solution; (3) the formation of the horseshoe structure and the direction of the tangential vector in that region.

Crow waves In the first test we start from a random perturbation and check the formation of Crow waves. We start from a small perturbation of a straight vortex separated by $b = 0.11$ and consider the evolution following Eq. (12) selecting $\varepsilon = 0.05$ and $r_c = 0.025$. The results are depicted in Fig. 4. We can see that at time $t = 2$ we have almost sinusoidal waves. The wavelength is around π that is very close to the value 0.98π predicted by formula (19) for the given values of ε, b and r_c.

Influence of the regularization parameter r_c The behavior of the vortices far from the reconnection is not dependent of r_c. However, at times when the vortices are close to each other the regularization parameter starts to play a crucial role. Furthermore, the evolution of vortices after reconnection also depends on the parameter r_c. We may expect that when the regularization parameter tends to zero, the shape of vortices will be less smooth. Therefore, the behavior of vortices after reconnection will resemble the behavior of a corner vortex. These expectations are confirmed by the numerical solution, see Figs. 5, 6 and 7.

We have consider a pair of symmetric vortices with initial conditions

$$\mathbf{X}(s, 0) = \begin{pmatrix} b - \delta\cos(s) \\ -\delta\cos(s) \\ s - \pi \end{pmatrix} \tag{42}$$

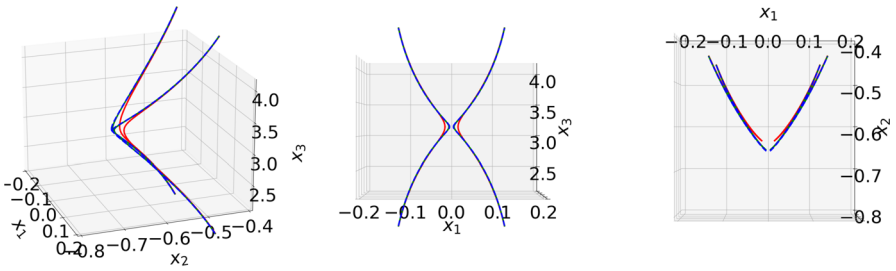

(a) 3D view (b) front view (c) top view

Fig. 5 Configuration of the vortices before the reconnection at time $t = 1.01$ for different r_c ($5 \cdot 10^{-3}$—red, $1.25 \cdot 10^{-3}$—green, $3.125 \cdot 10^{-4}$—blue) and $\varepsilon = 0.05$ (Color figure online)

where $b = \sqrt{\varepsilon}/2$, $\delta = b/20$, in the interval $(0, 2\pi)$ discretized with 6000 nodes. The boundary conditions are periodic. The parameter b is selected using formula (19) in such a way that there is exactly one Crow wave in the considered interval. If we decrease b the reconnection may happen in multiple points, thus complicating the analysis, whereas for larger values of b the reconnection does not happen due to the periodic boundary conditions. The computations until time $t = 1.5$ take around a day on a personal computer that is comparable with the performance of the solution of the Navier–Stokes equations from Sect. 1 on the same computer. The advantage is that now we can consider much thinner vortices and has 6000 nodes along the vortex instead of 320.

The vortices start to touch each other at time $t = 1.01$, Fig. 5. The influence of r_c can be notice only close to the reconnection region, and the shape of vortices is sharper for small r_c. It is not completely clear what we can call "the reconnection moment": the first touch or the moment when the horseshoe emerges. Both these moments are dependent on r_c. However, the second one has a more complicated dependence since the smallest size of the horseshoe is dictated by r_c: the smaller r_c, the smaller the horseshoe structure will be. This effect is demonstrated in Fig. 6 where the configuration of vortices at time $t = 1.025$ is depicted. We can see that even though for all r_c we have a contact the horseshoe appears only for small values of r_c. Furthermore, only for small values of the regularization parameter we can see the helical waves at this time moment. The fact that we cannot define the reconnection moment does not allow us to change the topology of vortices that leads to the formation of the bridge between the horseshoes. The bridge is growing and represents a source of numerical difficulties and possible instabilities at later times. The bigger bridge at time $t = 1.05$ can be seen in Fig. 7. There we can also see the horseshoe and the helical waves for large values of r_c. It is interesting to note that the difference between solutions for $r_c = 1.25 \cdot 10^{-3}$ and $r_c = 3.125 \cdot 10^{-4}$ is almost neglectable. We can expect that there is a convergence when r_c tends to zero.

The analysis of the influence of r_c to the solution shows an important phenomenon: the reconnection moment cannot be determined, so the "real corner" between vortices cannot be seen. We can see only the consequences, such as the horseshoe starting from some minimal size related to r_c. This effect also appears in the experiments

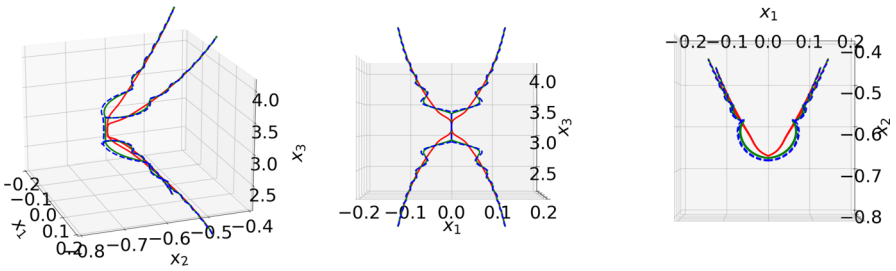

Fig. 6 Configuration of the vortices at time $t = 1.25$ when the horseshoe structure emerged for all r_c ($5 \cdot 10^{-3}$—red, $1.25 \cdot 10^{-3}$—green, $3.125 \cdot 10^{-4}$—blue) and $\varepsilon = 0.05$ (Color figure online)

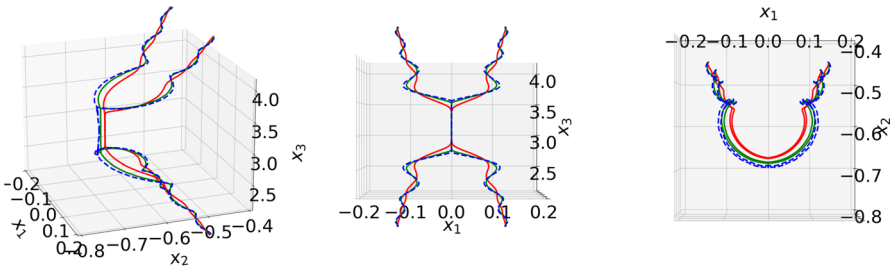

Fig. 7 Configuration of the vortices after the reconnection at time $t = 1.5$ for different r_c ($5 \cdot 10^{-3}$—red, $1.25 \cdot 10^{-3}$—green, $3.125 \cdot 10^{-4}$—blue) and $\varepsilon = 0.05$ (Color figure online)

(Fonda et al. 2019). Since the regularization parameter has the physical meaning of the radius of vortex core, we can expect that for thick vortices we will never see the singularity and the shape after the reconnection will be closer to a vortex ring without any helical waves, since the minimal size of the horseshoe is big and close to the length of Crow waves. When the vortices get thinner the shape after reconnection becomes more complicated. However, we still do not see the singularity. One of the challenges related to this phenomenon is the incapacity to perform the reconnection, that is to say the change topology, because we do not know when we have to do it. On the one hand if we reconnect the vortices when they touch each other, the corner they create is not the one that generates the horseshoe structure. On the other hand, if we wait until the horseshoe structure emerges we always find an artifact on its tip related to the bridge.

Influence of the parameter ε

The results obtained in Sect. 3 predict that the horseshoe will be closer to circular when the value of ε increases (formula (27)). We use same initial condition (42) as before but now the initial distance $b = \sqrt{\varepsilon}/2$, and the perturbation $\delta = b/20$ both depend on the parameter ε. It is necessary for two things: firstly, we have to use such initial distance, so there is at least one Crow wave in the interval; secondly, the change of perturbation amplitude allows to achieve the reconnection almost at the same time.

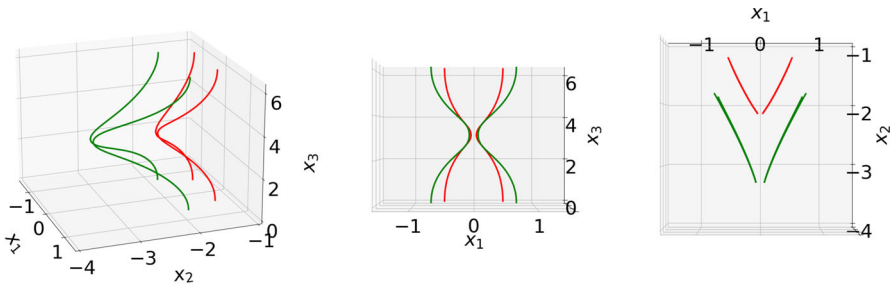

(a) 3D view (b) front view (c) top view

Fig. 8 Configuration of the vortices before the reconnection at time $t = 1.1$ for different ε ($\varepsilon = 0.5$—red, $\varepsilon = 1$—green) and $r_c = 0.05$ (Color figure online)

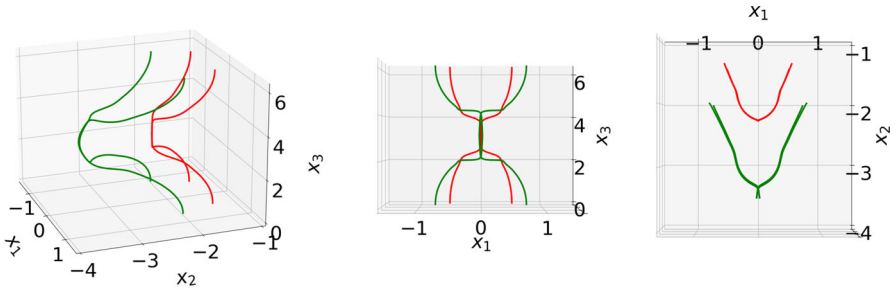

(a) 3D view (b) front view (c) top view

Fig. 9 Configuration of the vortices at time $t = 1.2$ when the horseshoe structure emerges for different ε ($\varepsilon = 0.5$—red, $\varepsilon = 1$—green) and $r_c = 0.05$ (Color figure online)

The regularization parameter is set to $r_c = 0.05$, and the interval $(0, 2\pi)$ is discretized with 6000 nodes.

The configuration of the vortices at different time moments is depicted in Figs. 8, 9 and 10. In the first figure the reconnection has not happened yet. However, we can see that the vortices with bigger values of ε move faster in x_2 direction and also the amplitude of Crow wave is bigger due to the bigger initial distance b. In Fig. 9 the moment when the horseshoe structure emerges is depicted, but there are still no helical waves. For the smaller value of ε the horseshoe structure is not planar and has a sharper tip. The configuration with helical waves and the horseshoe structure is shown in Fig. 10. For the large value of ε the horseshoe is almost planar and the vortices look very similar to the shape we can see in evolution of a corner vortex in Fig. 2.

Another important question one may ask is the behavior of the vortices around the reconnection. In particular, is there a cusp? Or can we expect a smooth horseshoe? In order to do it we can analyze the components of the tangential vector $\mathbf{T}$. The bigger value of the first component T_1 corresponds to a smoother horseshoe. Moreover, when $\mathbf{T}$ is parallel to $\mathbf{e}_1$ the cusp disappears. A very rough analytical result on the ratio $T_1/|\mathbf{T}|$ is presented in Sect. 3. Using numerical simulations we can see that the value of $T_1/|\mathbf{T}|$ may be very close to 1 for some ε. In Fig. 11a it is possible to see that

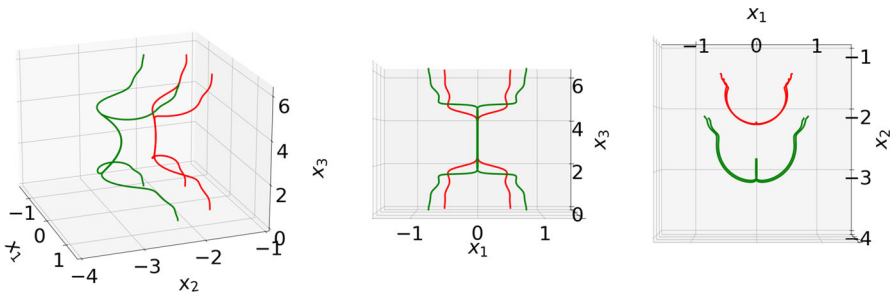

(a) 3D view (b) front view (c) top view

Fig. 10 Configuration of the vortices after the reconnection at time $t = 1.3$ for different ε ($\varepsilon = 0.5$—red, $\varepsilon = 1$—green) and $r_c = 0.05$ (Color figure online)

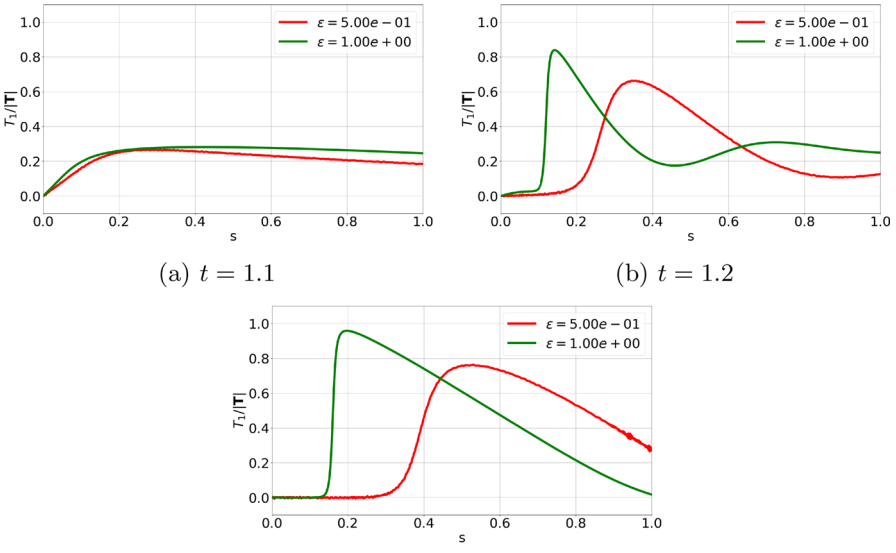

(a) $t = 1.1$ (b) $t = 1.2$

(c) $t = 1.3$

Fig. 11 The ration $T_1/\|\mathbf{T}\|$ for different time moments, different values of ε and $r_c = 0.05$

before the reconnection the projection of normalized vector $\mathbf{T}$ to the direction $\mathbf{e}_1$ is small because it is mostly oriented in the $\mathbf{e}_3$ direction. However, in Fig. 11b when the reconnection already happens we can see that there is a bridge, where T_1 is close to 0, and a jump almost of size 1 at tip of the horseshoe. Moreover, the bigger is ε the bigger is the maximum of $T_1/|\mathbf{T}|$. This coincides with the analytical result from Sect. 3. In Fig. 11c we can see that the bridge is growing and the horseshoe persists.

6 Comparison with the Eye-Shaped Vortex

We can compare the evolution of the reconnected vortices with an isolated vortex which has an eye-shape and deforms obeying the local induction approximation. These not planar vortex can be considered as an approximation of the shape after reconnection (see Fig. 1c) or as a "two-corner curvilinear polygon". We will see that the evolution of the eye-shaped vortex has similarities with both the reconnection process and the evolution of polygonal vortex. It means that even though we cannot see the corner at the reconnection time, the further evolution of the vortices has a similar structure to the corner vortex (Fig. 2) under LIA.

It is known Hoz and Vega (2018), Jerrard and Smets (2015) that a polygonal vortex with M corners has a periodic behavior with period $T = 2\pi/M^2$, whereas the trajectory of the corner tends to a modification of Riemann's non-differential function (RNDF):

$$\mathcal{R}(t) = \sum_{k=1}^{\infty} \frac{e^{itk^2}}{k^2} \tag{43}$$

when M tends to infinity, $i^2 = -1$. RNDF is a periodic multifractal that has a peculiar behavior at points corresponding to rational multiples of the period (Banica and Vega 2022). It can be seen in Fig. 12. We pick a point $t^* = \pi/4$ and multiply it by different rational numbers. It is easy to see that most of them correspond to local minima and maxima of the absolute value of (43) and to corners of the graph in the complex plane. However, points that correspond to the rational multiples with odd denominator fall into a cusp singularity of the absolute value of RNDF seen as a spiral on the complex plane. It was shown in Hoz and Vega (2018) that the polygonal vortices have a similar behavior. Furthermore, at each rational multiple p/q of the period the shape of the corresponding vortex is also polygonal though not necessary planar. Moreover, the angle between two adjacent sides tends to π when q tends to infinity. This dependence on q is more visible in the H_δ process studied in Kumar et al. (2022).

The similar effect can be seen for the eye-shaped vortex which can be considered as a curvilinear polygon with two corners. The eye-shaped vortex is more similar to the configuration we have after the reconnection than a polygonal one; therefore, the comparison with it is interesting to us. In "Appendix C" it is shown that the evolution of this vortex is quasi-periodic. Moreover, the Fourier analysis of the trajectory that starts in a corner shows that the dominating frequencies are still the squares like in the polygonal case.

The fluid impulse of the reconnected vortices We define the fluid impulse around the corner as

$$\mathcal{F}_l(t) = \frac{1}{2}\int_{-l/2}^{l/2} (\mathbf{X}(q,t) - \mathbf{X}_0(t)) \wedge \mathbf{X}_s(q,t)dq, \tag{44}$$

where the corner is located at $s = 0$ and the interval l is 20% of the whole perimeter of the vortex. The fluid impulse is important for us because in the case of the reconnection we cannot extract the singularity point; hence, we cannot find its trajectory, whereas formula (44) is always applicable. It depends however on the position of the origin $\mathbf{X}_0$

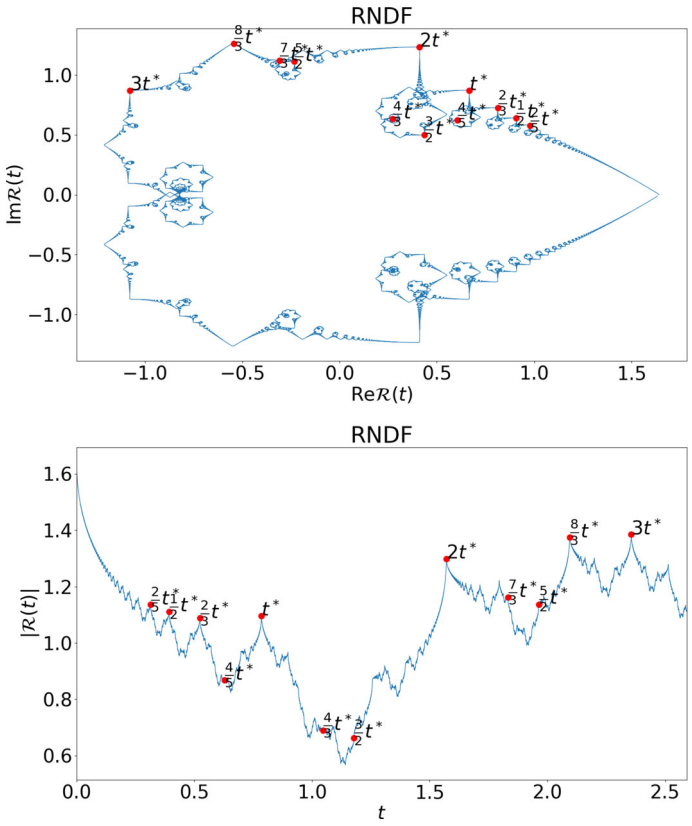

Fig. 12 Riemann's non-differential function (43) on the complex plane and its absolute value

which in the case of the eye-shaped vortex we define as $\mathbf{X}_0(t) = \mathbf{X}(0, t)$. We will be mainly interested in the oscillations and multi-fractal behavior for which the choice of origin does not have any influence.

Despite this similarity to the RNDF, the real structure of the fluid impulse of the eye-shaped vortex is much more complicated, as can be seen in Fig. 13. The curve is still planar since $\mathcal{F}_1(t) = 0$ for all time, the rational multiples of a local maxima $t^* = 0.10848$ also correspond to the local maxima, minima and singular points, but the scaling of self-similar structures is deformed and there is no real period. The dependence on the size of the maxima with respect to the size of the denominator is also presented.

In the case of the reconnection we cannot specify the reconnection point and follow its trajectory. However, we can calculate fluid impulse (44) around the reconnection region. The results for different r_c and $\varepsilon = 0.05$ are depicted in Fig. 14. Analyzing the fluid impulse we can detect a sudden change from monotone to oscillating behavior at time $t \approx 1.01$. We call this moment the reconnection time. Note that from the configuration of the vortices we could not to define this time; thus, analysis of integral quantities such as the fluid impulse is beneficial for understanding of the reconnection

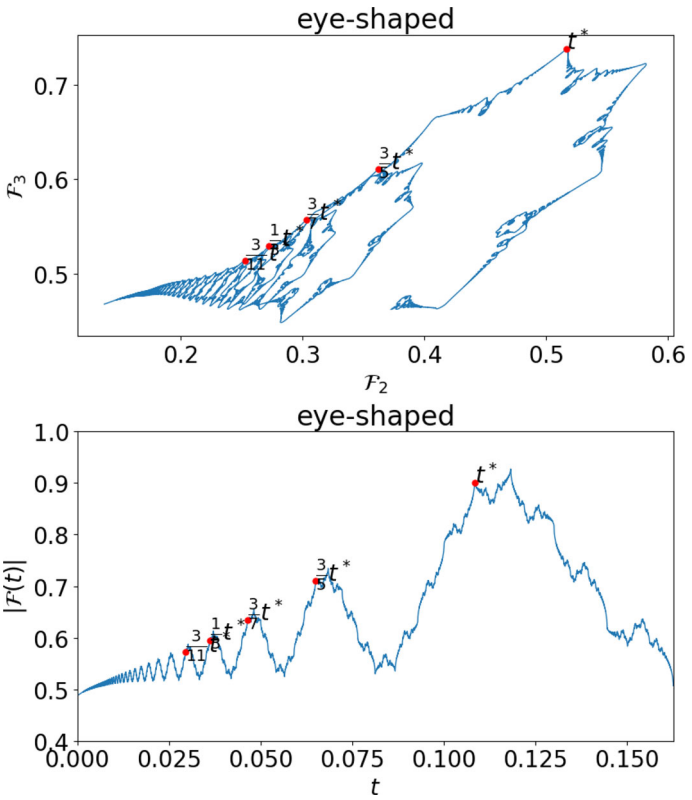

Fig. 13 Fluid impulse of an eye-shaped vortex for $b = 0.4$, $\theta = \pi/6$ and its modulus. Some maxima a located in times $3/11t^*$, $1/3t^*$, $3/7t^*$, $3/5t^*$, t^*, and the bigger is the denominator, the smaller is the peak at that (similar to what happens in Kumar et al. 2022)

phenomena. Moreover, one can note that the behavior after the reconnection time is quite reminiscent to the one of the eye-shaped vortex though the period is different. The smaller is the regularization parameter r_c, the more details we can see in the fluid impulse.

The extraction of squares however is not possible for the reconnection problem due to the noise generated by the bridge. Analysis of distribution of minima, maxima, and singular points using wavelet transform has also faced problems related to the noise. Maxima for the considered types of signals correspond to singular points that can be studied using the multifractal analysis (Turiel et al. 2006; Muzy et al. 1993). The main idea of this approach is to construct the singularity spectrum $D(h)$, that is the function for which each Hölder exponent h yields the Hausdorff dimension of the set of points where the function has this exponent. For RNDF the singularity spectrum is known: $D(h) = 4h - 2$ for $h \in [0.5, 0.75]$, $D(h) = 0$ for $h = 1.5$ and $D(h) = -\infty$ otherwise Jaffard (1996). We have tried to use the p-leaders method (Wendt et al. 2007) to estimate the spectrum of RNDF and the fluid impulse. Unfortunately these signals are quite delicate. Therefore, even in the case of RNDF the approximation of $D(h)$ is not very accurate (especially for exponents corresponding to $D(h) = 0$). For

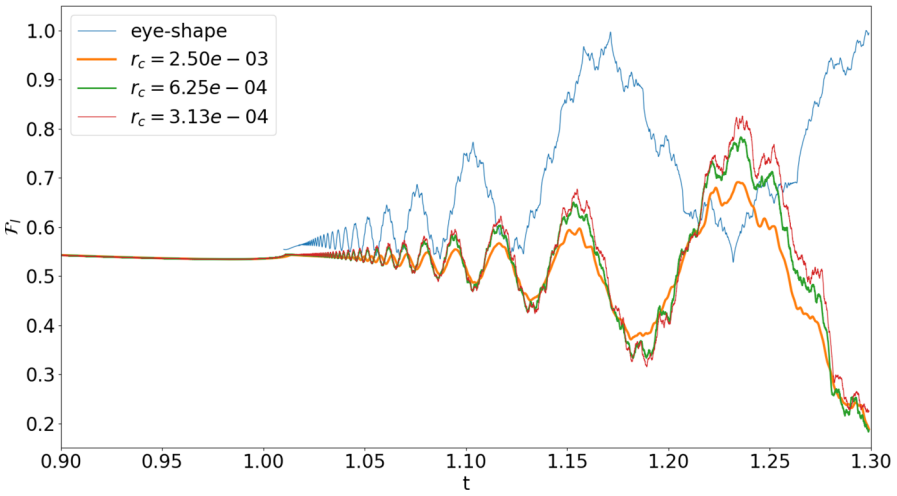

Fig. 14 Fluid impulse (44) for the reconnection problem with different values of r_c, $\varepsilon = 0.05$, and $b = \sqrt{\varepsilon}$. The blue line corresponds to normalized and shifted fluid impulse of the eye-shaped vortex with $\theta = \pi/6$ and $b = 0.4$. At time $t \approx 1.01$ the behavior suddenly changes from monotone growth to oscillation. We can use it as the definition of the reconnection time

the fluid impulse of the polygonal or reconnected vortices the situation is much worse even though there is a tendency that h corresponding to maximal $D(h)$ is decreasing getting closer to 0.75.

Since the multifractal analysis failed, in this paper we perform only a qualitative analysis of similarity between the fluid impulse of the eye-shaped vortex and the one of the reconnection problem. We choose a point t^* related to a local maxima of the reconnection fluid impulse and check whether the rational multiples of this point also fall in maxima, minima or singular points. The results are depicted in Fig. 15 for $\varepsilon = 0.03$, $b = 0.22$, $r_c = 6.25 \cdot 10^{-4}$. We can see that the rational points mostly fall into local minima and maxima at least for a short time after reconnection. However later we can see that the self-similar structure of the fluid impulse vector is completely lost. In order to obtain a cleaner structure we have to focus on a small time interval after the reconnection and choose a small regularization parameter r_c. This is quite challenging, due to stability condition (36) of the method. Thus, a new approach is required to find more similarities between the reconnection process and the eye-shaped vortex.

The vortex separation rate he scaling law which determines how the distance between vortices changes during the reconnection was studied in multiple works (Villois et al. 2017; Fonda et al. 2019; Yao and Hussain 2020). It is not completely clear whether there are different laws before and after the reconnection or whether this law varies for quantum and classical fluids. Nevertheless, there are multiple evidences that the separation rate $\delta(t)$ of the vortices after the reconnection should be of the scale $\sqrt{t - t_{rec}}$ where t_{rec} is the reconnection time. This rate can be observed in experiments (Fonda et al. 2019) and also coincide with the analytical result for the corner vortex (Gutiérrez 2003).

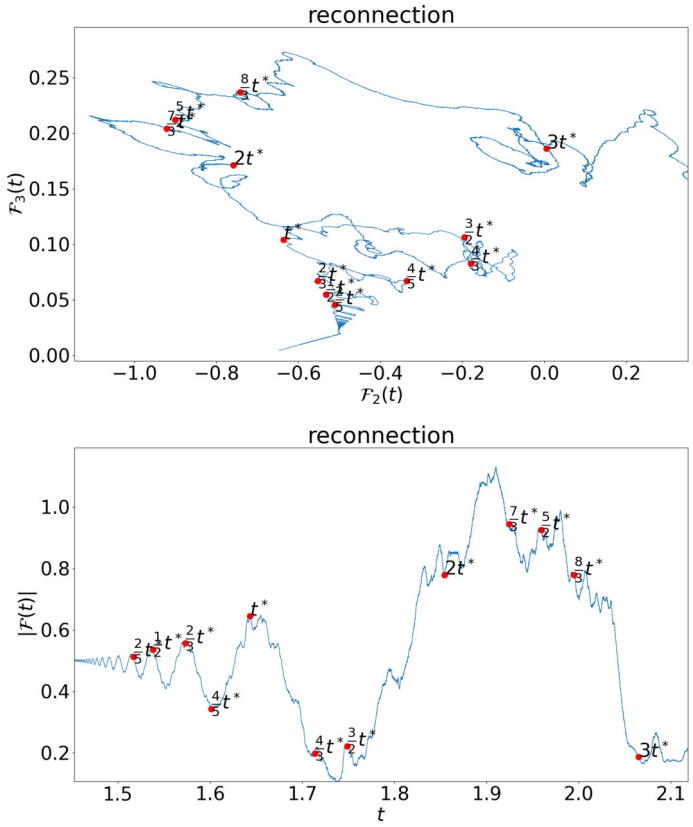

Fig. 15 Fluid impulse and its modulus for the reconnection problem when $\varepsilon = 0.03$, $b = 0.22$, $r_c = 6.25 \cdot 10^{-4}$

In Fig. 16 the separation rates before and after the reconnection are depicted for $\varepsilon = 0.05$ different values of r_c. The black dashed lines correspond to the scale $\sqrt{|t - t_{rec}|}$. We can see that before and after the reconnection the separation rate is very close to the square root law. The agreement is better for small values of r_c that correspond to a case of smaller viscosity. We can also note that the x_2 component of the position of the eye-shaped vortex corner has the same square root timescale as the reconnected vortices (Fig. 16b). This result can be considered as another evidence that the behavior of the vortices after the reconnection resembles the evolution of the corner vortex even though we cannot see the corner at the reconnection time due to the presence of the regularization parameter r_c.

7 Conclusions

Even though it is not entirely clear what happens in the reconnection time the further evolution of vortices contains coherent structures reminiscent to the ones generated by a polygonal vortex (Hoz and Vega 2018; Jerrard and Smets 2015). In order to extract

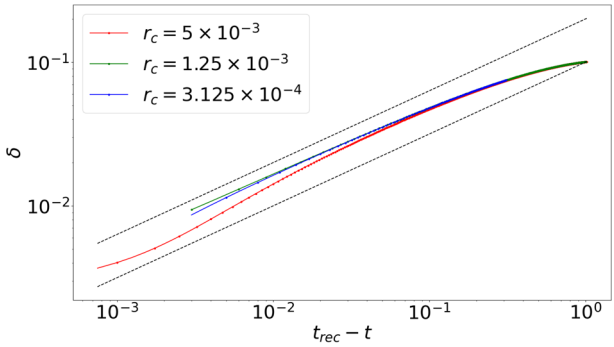

(a) Before the reconnection

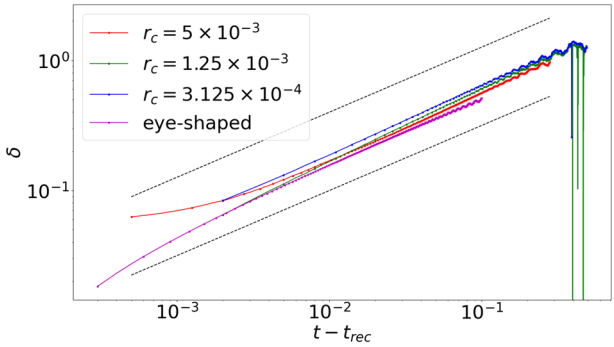

(b) After the reconnection

Fig. 16 The minimal distance between vortices before and after the reconnection for $\varepsilon = 0.05$ and different values of r_c

and analyze these structures new model (12) describing the interaction of a pair of antiparallel vortices is developed. The introduction of the regularization parameter r_c allows us to go beyond the reconnection time. Moreover, the model provides closed expression (22) for the length of the tangent vector of the vortex central line. This length is proportional to the circulation, and according to our result, it is increasing, when the distance between vortices tends to 0. It can be considered as the vortex stretching phenomenon. The model also predicts the Crow waves firstly described in Crow (1970) and the formation of coherent structures. These structures are a pair of horseshoes in the spirit of Schwarz (1985), Gutiérrez (2003) connected by a bridge which is artificial but cannot be removed due to restrictions of the model. Nevertheless, we have shown analytically in Sect. 3 that the non-smoothness of the horseshoe due to the bridge can be bounded. Finally, the model predicts the square root timescale for the separation rate after the reconnection.

We performed a numerical simulation for different values of the vortex interaction parameter ε and the regularization parameter r_c. There is a difference with the evolution of the corner vortex filament shown in Fig. 2 and the reconnection. In the first case the horseshoe emerges immediately and can be infinitely small, whereas for our model the smallest possible size of the horseshoe is finite and dictated by the parameter r_c.

This effect makes impossible to determine the reconnection time, so we can speak only about the reconnection interval which is getting smaller when r_c tends to zero. However, the reconnection time can be defined better if an integral quantity instead of the configuration of the vortices is considered. We focus on the fluid impulse that is an integral of the cross-product between the position and the vorticity calculated in the reconnection region. It is possible to see a sudden change of the behavior of this quantity from monotone to oscillatory happening at the reconnection time (see Fig. 14). Note also that the smaller r_c the more complicated the behavior after the reconnection is. The oscillations look quite reminiscent to the ones of the fluid impulse of the polygonal vortex (Hoz and Vega 2018) that it tends to Riemann's non-differential function (RNDF, formula (43)) when the number of polygon sides tends to infinity. It can be considered as an evidence that the antiparallel vortices indeed form a corner at the reconnection. However, a further research is necessary for estimation of the noise produced by the bridge, studying the influence of the interaction, and calculation of the corner angle.

A possible way to find more similarities between the fluid impulse of reconnecting vortices and RNDF is to improve the numerical method. In particular condition (36) is very restrictive because we have to reduce both space and time discretization to be able to solve problems with small r_c. Probably this restriction can be surpassed by choosing right orders in space and time discretizations. Another way is to apply filtering to the already obtained fluid impulse or try more advanced methods of the analysis. We have tried to apply methods of multifractal analysis such as the p-leader method (Wendt et al. 2007). This approach is based on studying the distribution of the singular points of the function and the calculation of the singularity spectrum which can be considered as a fingerprint of the signal. Similar singularity spectrum means similar multifractal properties of the signals. Since the RNDF is very delicate for such methods, and the fluid impulse of the reconnecting vortices has a lot of noise, our analysis could not arrive to any conclusion.

Advances in the study of the vortex reconnection may have a huge impact to the understanding of turbulence and its structure.

Funding Open Access funding provided thanks to the CRUE-CSIC agreement with Springer Nature.

Appendix A: Equations in the Generalized Frenet Frame

Equation (12) can also be rewritten in the generalized Frenet frame following (Hou et al. 1998). In this part in we use **T** to designate the normalized tangential vector, not

just the derivative $\mathbf{X}_s$. Consider the orthonormal frame in $\mathbb{R}^3$:

$$\mathbf{T} = \frac{\mathbf{X}_s}{|\mathbf{X}_s|}, \quad \mathbf{N}_1 \perp \mathbf{T}, \quad \mathbf{N}_2 = \mathbf{T} \wedge \mathbf{N}_1. \tag{45}$$

For this frame we can write the generalized Frenet system:

$$\frac{\partial}{\partial q}\mathbf{T} = \kappa_1 \mathbf{N}_1 - \kappa_2 \mathbf{N}_2, \tag{46}$$

$$\frac{\partial}{\partial q}\mathbf{N}_1 = -\kappa_1 \mathbf{T} + \omega \mathbf{N}_2, \tag{47}$$

$$\frac{\partial}{\partial q}\mathbf{N}_2 = \kappa_2 \mathbf{T} - \omega \mathbf{N}_1, \tag{48}$$

where q is the arclength parameter, that is $\frac{\partial}{\partial q} = \frac{1}{|\mathbf{X}_s|}\frac{\partial}{\partial s}$. In terms of system (46)–(48) the curvature and the torsion can be calculated as

$$\kappa = \sqrt{\kappa_1^2 + \kappa_2^2}, \tag{49}$$

$$\tau = \omega + \frac{\kappa_2 \kappa_{1,q} - \kappa_1 \kappa_{2,q}}{\kappa^2}, . \tag{50}$$

On the other hand the vectors $\mathbf{T}$, $\mathbf{N}_1$ and $\mathbf{N}_2$ change in time following the system

$$\frac{\partial}{\partial t}\mathbf{T} = -\lambda_1 \mathbf{N}_2 + \lambda_2 \mathbf{N}_1, \tag{51}$$

$$\frac{\partial}{\partial t}\mathbf{N}_1 = -\lambda_2 \mathbf{T} + \lambda_3 \mathbf{N}_2, \tag{52}$$

$$\frac{\partial}{\partial t}\mathbf{N}_2 = \lambda_1 \mathbf{T} - \lambda_3 \mathbf{N}_1. \tag{53}$$

We can recover coefficients λ_i, $i \in \{1, 2, 3\}$ using Eq. (12). Indeed, in frame (45) final system (12) reads

$$\mathbf{X}_t = u\mathbf{N}_1 + v\mathbf{N}_2, \tag{54}$$

where coefficients are given by

$$u = \kappa_2 + \varepsilon \frac{x_1}{x_1^2 + r_c^2} n_2, \tag{55}$$

$$v = \kappa_1 - \varepsilon \frac{x_1}{x_1^2 + r_c^2} n_1. \tag{56}$$

Here n_1 and n_2 are first components of the vectors $\mathbf{N}_1$ and $\mathbf{N}_2$, respectively. Taking derivative of (54) respect to s we obtain

$$\mathbf{X}_{st} = \mathbf{T}L(-u\kappa_1 + v\kappa_2) + \mathbf{N}_1(u_s - L\omega v) + \mathbf{N}_2(v_s + L\omega u), \tag{57}$$

where $L = |\mathbf{X}_s|$. On the other hand we can write that $\mathbf{X}_s = L\mathbf{T}$ and take derivative with respect to t:

$$\mathbf{X}_{st} = L_t\mathbf{T} + \lambda_2 L\mathbf{N}_1 - \lambda_1 L\mathbf{N}_2. \tag{58}$$

Since for $\mathbf{X}(s,t)$ the order of differentiation does not matter, we can find the equation for L_t:

$$L_t = L(-u\kappa_1 + v\kappa_2), \tag{59}$$

and also expressions for coefficients λ_1 and λ_2:

$$\lambda_1 = -\frac{v_s}{L} - \omega u, \tag{60}$$

$$\lambda_2 = \frac{u_s}{L} - \omega v. \tag{61}$$

We can continue this process and obtain the equations for $\kappa_{1,t}$ and $\kappa_{2,t}$:

$$\kappa_{1,t} = \frac{1}{L}\frac{\partial}{\partial s}\left(\frac{u_s}{L}\right) - \frac{\omega_s v + 2\omega v_s}{L} - \omega^2 u + \kappa_1(u\kappa_1 - v\kappa_2) - \lambda_3\kappa_2, \tag{62}$$

$$\kappa_{2,t} = -\frac{1}{L}\frac{\partial}{\partial s}\left(\frac{v_s}{L}\right) - \frac{\omega_s u + 2\omega u_s}{L} + \omega^2 v + \kappa_2(u\kappa_1 - v\kappa_2) + \lambda_3\kappa_1. \tag{63}$$

What do we need to close the system? In the expression for u and v we use x_1, n_1 and n_2 whose equations can be obtained from (54), (52), and (53), respectively:

$$x_{1,t} = un_1 + vn_2, , \tag{64}$$

$$n_{1,t} = -\left(\frac{u_s}{L} - \omega v\right)\frac{x_{1,s}}{L} + \lambda_3 n_2, \tag{65}$$

$$n_{2,t} = -\left(\frac{v_s}{L} + \omega u\right)\frac{x_{1,s}}{L} - \lambda_3 n_1. \tag{66}$$

Here we got rid of λ_1 and λ_2 using (60), (61). Expressions for ω and λ_3 are still missing. There are two ways to find the first quantity. First one is to use equations (47) and (48):

$$\omega = \frac{n_{1,s}n_2 + \kappa_1 x_{1,s}n_2 - n_{2,s}n_1 + \kappa_2 x_{1,s}n_1}{L(n_1^2 + n_2^2)}. \tag{67}$$

This is a functional equation, and it does not include λ_3. However, in order the denominator to be nonzero we have to require $n_1^2 + n_2^2 \neq 0$ that is $\mathbf{T} \neq \mathbf{e}_1$. Another way is to take a derivative of (47) respect to t and a derivative of (52) respect to q making them equal that gives a differential equation for ω_t:

$$\omega_t = \frac{u_s\kappa_2 + v_s\kappa_1 + \lambda_{3,s}}{L} + \omega(-v\kappa_2 + u\kappa_1). \tag{68}$$

In order to find λ_3 we have to make assumptions about our frame. Suppose that $n_2 = 0$ and use Eq. (66):

$$\lambda_3 = -\left(\frac{v_s}{L} + \omega u\right)\frac{x_{1,s}}{Ln_1} = -\left(\frac{v_s}{L} + \omega u\right)\frac{x_{1,s}}{\sqrt{L^2 - x_{1,s}^2}}. \tag{69}$$

Then the direct expressions for $\mathbf{N}_1$ and $\mathbf{N}_2$ are:

$$\mathbf{N}_1 = \frac{T_1\mathbf{T} - \mathbf{e}_1}{\sqrt{1 - T_1^2}}, \quad \mathbf{N}_2 = \frac{\mathbf{e}_1 \wedge \mathbf{T}}{\sqrt{1 - T_1^2}}.$$

To make the first vector not zero the tangential vector should not be oriented in the $\mathbf{e}_1$ direction. Numerical experiments show that if $r_c > 0$ this is true before the reconnection and a long time after it. The second vector corresponds to the direction of the interaction term in system (12). This choice of frame vectors has another advantage that we can express κ_1 using L, x_1 and their derivatives. Indeed, calculating inner product of (46) with $\mathbf{N}_1$ and taking into account that $\mathbf{T}_q \cdot \mathbf{T} = 0$ we obtain:

$$\kappa_1 = \frac{1}{\sqrt{L^2 - x_{1,s}^2}}\frac{\partial}{\partial s}\left(\frac{x_{1,s}}{L}\right), \quad \omega = \frac{\kappa_2 x_{1,s}}{\sqrt{L^2 - x_{1,s}^2}}. \tag{70}$$

Using this we can reduce the system of equations to only 3 unknowns:

$$x_{1,t} = -\kappa_2\sqrt{L^2 - x_{1,s}^2}, \tag{71}$$

$$L_t = L\varepsilon\frac{x_1}{x_1^2 + r_c^2}\kappa_2\sqrt{L^2 - x_{1,s}^2}, \tag{72}$$

$$\kappa_{2,t} = -\frac{1}{L}\frac{\partial}{\partial s}\left(\frac{v_s}{L}\right) - \frac{\omega_s u + 2\omega u_s}{L} + \omega^2 v + \kappa_2(u\kappa_1 - v\kappa_2) + \lambda_3\kappa_1. \tag{73}$$

We will show later that Eq. (72) can be resolved analytically. Besides, similarly to κ_1 we can find κ_2

$$\kappa_2 = \frac{Lx_{1,t}}{\sqrt{L^2 - x_{1,s}^2}},$$

and see that it is proportional to the velocity $x_{1,t}$. Thus, the behavior of the system of antiparallel vortices is governed by 2 quantities: the distance between vortices x_1 and the velocity of their approximation represented by κ_2.

Even though the choice of the interaction frame allows us to reduce the number of unknowns, it is not very useful in numerical simulation since the 4th derivative of x_1 respect to s is required: Eq. (73) includes the second derivative of v, that according to (56) depends on κ_1, that is proportional to the second derivative of x_1 due to (70). In practice, it is better to use initial formulation (12).

Appendix B: Algorithm for the Numerical Solution

Assume that at time $t = t_0$ the initial values $\mathbf{X}, \mathbf{T}$ are given. Suppose also that we know function $L_0(s)$ from Eq. (22) and its derivative $L_0'(s)$. We use the following algorithm to obtain the numerical solution up to the time t_{end} with space discretization step h and time step Δt:

while $t < t_{\text{end}}$ **do**
  accuracy_test_passed $\leftarrow$ False
  while accuracy_test_passed is False **do**
    $\Delta\mathbf{X} \leftarrow \mathbf{0}$; $\Delta\mathbf{T} \leftarrow \mathbf{0}$
    $\mathbf{X}_{\text{error}} \leftarrow \mathbf{0}$; $\mathbf{T}_{\text{error}} \leftarrow \mathbf{0}$
    for $k \leftarrow 1$ to 6 **do**
      $\boldsymbol{\xi} \leftarrow \mathbf{X}$; $\boldsymbol{\tau} \leftarrow \mathbf{T}$
      for $q \leftarrow 1$ to $k-1$ **do**
        $\boldsymbol{\xi} \leftarrow \boldsymbol{\xi} + \Delta t\ \alpha_{k-1,q}\ \mathbf{X}^{(q)}$; $\boldsymbol{\tau} \leftarrow \boldsymbol{\tau} + \Delta t\ \alpha_{k-1,q}\ \mathbf{T}^{(q)}$
      end for
      $\boldsymbol{\tau}_{s,h} \leftarrow$ FirstDerivative($\boldsymbol{\tau}, h$)
      $\boldsymbol{\tau}_{ss,h} \leftarrow$ SecondDerivative($\boldsymbol{\tau}, h$)
      $a \leftarrow L_0(\xi_1^2 + r_c^2)^{-\varepsilon/2}$ // modulus of tangential vector (22)
      $b \leftarrow \frac{L_0'}{L_0} - \varepsilon \frac{\xi_1}{\xi_1^2 + r_c^2} \tau_1$ // correction $|\boldsymbol{\tau}|_s / |\boldsymbol{\tau}|$
      $\mathbf{X}^{(k)} \leftarrow \frac{\boldsymbol{\tau} \wedge \boldsymbol{\tau}_{s,h}}{a^3} - \frac{\varepsilon \xi_1}{a(\xi_1^2 + r_c^2)} \boldsymbol{\tau} \wedge \mathbf{e}_1$
      $\mathbf{T}^{(k)} \leftarrow \frac{\boldsymbol{\tau} \wedge (\boldsymbol{\tau}_{ss,h} - 3b\boldsymbol{\tau}_{s,h})}{a^3} - \frac{\varepsilon \tau_1 (r_c^2 - \xi_1^2)}{a(\xi_1^2 + r_c^2)^2} \boldsymbol{\tau} \wedge \mathbf{e}_1 - \frac{\varepsilon \xi_1}{a(\xi_1^2 + r_c^2)} \left(\boldsymbol{\tau}_{s,h} - b\boldsymbol{\tau}\right) \wedge \mathbf{e}_1$
      $\Delta\mathbf{X} \leftarrow \Delta\mathbf{X} + \Delta t\ c_k\ \mathbf{X}^{(k)}$; $\Delta\mathbf{T} \leftarrow \Delta\mathbf{T} + \Delta t\ c_k\ \mathbf{T}^{(k)}$
      $\mathbf{X}_{\text{error}} \leftarrow \mathbf{X}_{\text{error}} + \Delta t\ \hat{c}_k\ \mathbf{X}^{(k)}$; $\mathbf{T}_{\text{error}} \leftarrow \mathbf{T}_{\text{error}} + \Delta t\ \hat{c}_k\ \mathbf{T}^{(k)}$
    end for// $k \leftarrow 1$ to 6
    error $\leftarrow h\sqrt{\|\mathbf{X}_{\text{error}}\|^2 + \|\mathbf{T}_{\text{error}}\|^2}$
    if error $<$ threshold **then**
      accuracy_test_passed $\leftarrow$ True
      $\mathbf{X} \leftarrow \mathbf{X} + \Delta\mathbf{X}$
      $\mathbf{T} \leftarrow \mathbf{T} + \Delta\mathbf{T}$
      $t \leftarrow t + \Delta t$
    end if
    $\Delta t_{\text{new}} \leftarrow 0.9\Delta t \left(\frac{\text{threshold}}{\text{error}}\right)^{0.2}$
    $\Delta t \leftarrow 2^{\lfloor \log_2(\Delta t_{\text{new}}/\Delta t) \rfloor} \Delta t$
  end while// accuracy test not passed
end while// $t < t_{\text{end}}$

The coefficients a_{kq}, c_k and $\hat{c}_k$ are given in Butcher Table 1.

Table 1 Butcher table for Runge–Kutta–Fehlberg method (Fehlberg 1969)

2/9	2/9				
1/3	1/12	1/4			
3/4	69/128	−243/128	135/64		
1	−17/12	27/4	−27/5	16/15	
5/6	65/432	−5/16	13/16	4/27	5/144
	1/9	0	9/20	16/45	1/12
	47/450	0	12/25	32/225	1/30

Appendix C: The Eye-Shaped Vortex

The initial configuration of the eye-shaped vortex is given by

$$\mathbf{X}(s,0) = \begin{pmatrix} b\sin s \\ s - \pi/2 \\ -b\sqrt{\frac{1+\cos\theta}{1-\cos\theta} - \frac{1}{b^2}}\cos s \end{pmatrix}, \quad s \in (0,\pi], \tag{74}$$

where b is the thickness of the eye, θ is the angle of the corner, and the part $s \in (\pi, 2\pi]$ is obtained by reflection respect to the plane $x = 0$. Note that the component x_3 is real only if the expression below square root is positive; therefore, for large angles θ we also have to use a large separation b.

The evolution of eye-shape vortex (74) with $\theta = \pi/6$ and $b = 0.4$ is shown in Fig. 17. It is possible to see that the movement is quasi-periodic with period $T = 3.55$ since at that time we see that the vortex has again the eye-shape with the same orientation (blue line) but a slightly different parameters than at the initial time (red dashed line). We can also see that at a half-period time the vortex also has an eye-shape but is rotated (green line) similarly to the polygonal vortex (Hoz and Vega 2018). At a rational fraction p/q of the quasi-period T we can also see a non-planar curve with q

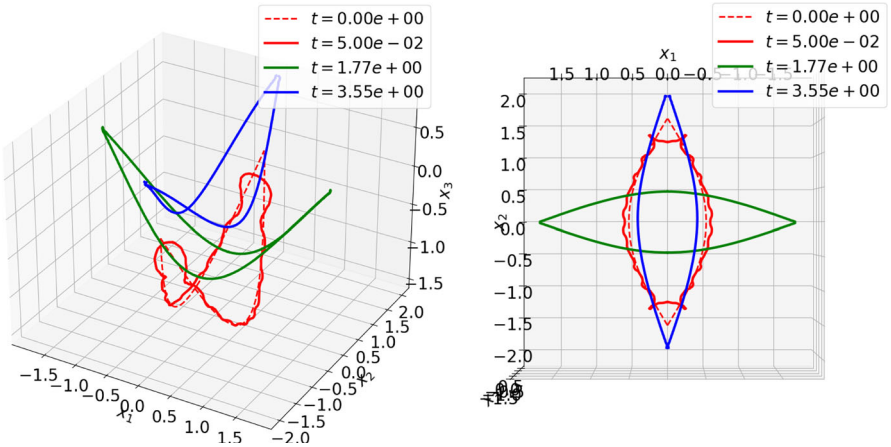

Fig. 17 Eye-shaped vortex (74) with $\theta = \pi/6$ and $b = 0.4$ at different time moments

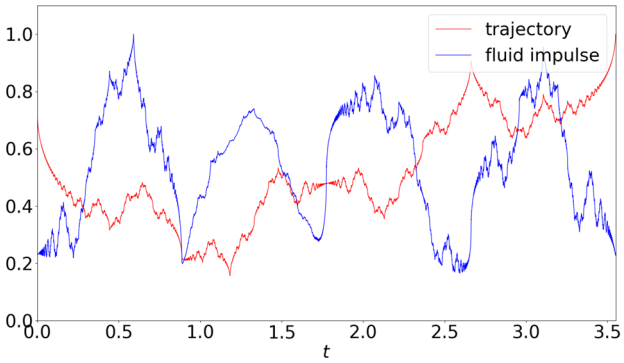

(a) Trajectory of the corner $\mathbf{X}(0,t)$ and fluid impulse around the corner (44)

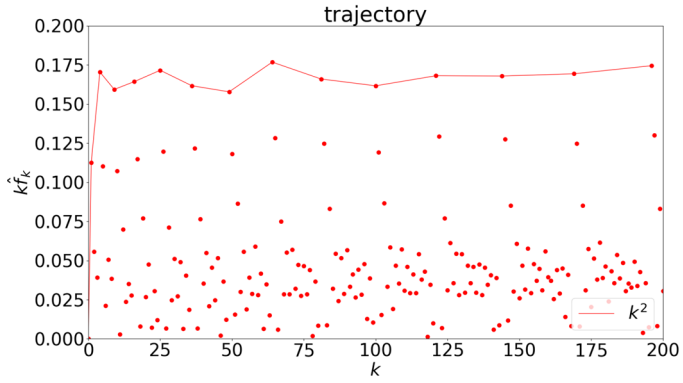

(b) Fourier coefficients of the trajectory

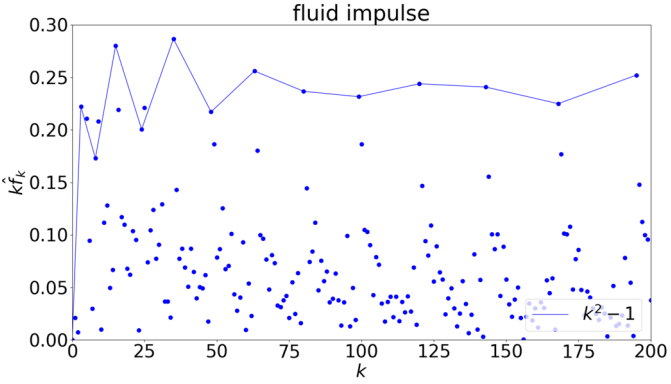

(c) Fourier coefficients of the fluid impulse

Fig. 18 Trajectory, fluid impulse and their Fourier coefficients for the eye-shaped vortex with $\theta = \pi/6$ and $b = 0.4$; the lines connect frequencies corresponding to squares of integers

or $2q$ corners for even and odd values of q, respectively. This behavior also coincides with the one of a polygon.

In Fig. 18a the trajectory of the corner $\mathbf{X}(0, t)$ and the fluid impulse around the corner are depicted. Analyzing the Fourier coefficients (Fig. 18b, c) we can see that for both the trajectory and the fluid impulse the frequencies corresponding to squares of integers are dominating similarly to what happens in the case of regular polygons (Hoz and Vega 2018). It makes the behavior similar to RNDF (43).

References

Banica, V., Vega, L.: Riemann's non-differentiable function and the binormal curvature flow. Arch. Ration. Mech. Anal. **244**, 501–540 (2022). https://doi.org/10.1007/s00205-022-01769-1

Banica, V., Faou, E., Miot, E.: Collision of almost parallel vortex filaments. Pure Appl. Math. (2017). https://doi.org/10.1002/cpa.21637

Bewley, G.P., et al.: Characterization of reconnecting vortices in superfluid helium. PNAS (2008). https://doi.org/10.1073/pnas.0806002105

Brenner, M.P., Hormoz, S., Pumir, A.: Potential singularity mechanism for the Euler equations. Phys. Rev. Fluids (2016). https://doi.org/10.1103/PhysRevFluids.1.084503

Butcher, J.C.: Numerical Methods for Ordinary Differential Equations. Wiley, New York (2008)

Buttke, T.F.: A numerical study of superfluid turbulence in the self-induction approximation. Ph.D. Thesis. University of California, Berkeley (1986)

Crow, S.C.: Stability theory for a pair of trailing vortices. AIAA J. **8**(12), 2172–2179 (1970). https://doi.org/10.2514/3.6083

De la Hoz, F., Vega, L.: Vortex filament equation for a regular polygon. Nonlinearity **27**(12), 3031 (2014)

De la Hoz, F., Vega, L.: On the relationship between the one-corner problem and the M-corner problem for the vortex filament equation. J. Nonlinear Sci. (2018). https://doi.org/10.1007/s00332-018-9477-7

Fehlberg, E.: Low-order classical Runge–Kutta formulas with stepsize control and their application to some heat transfer problem. National Aeronautics and Space Administration, vol. 315 (1969)

Fonda, E., Sreenivasan, K.R., Lathrop, D.P.: Reconnection scaling in quantum fluids. PNAS **116**(6), 1924–1928 (2019). https://doi.org/10.1073/pnas.1816403116

Gutiérrez, S., Rivas, J., Vega, L.: Formation of singularities and self-similar vortex motion under the localized induction approximation. Commun. PDEs **28**, 927–968 (2003)

Han, J., et al.: Large Eddy simulation of aircraft wake vortices within homogeneous turbulence: crow instability. AIAA J. (2000). https://doi.org/10.2514/2.956

Hou, T.Y., Klapper, I., Si, H.: Removing the stiffness of curvature in computing 3-D filaments. J. Comp. Phys. **143**, 628–664 (1998). https://doi.org/10.1006/jcph.1998.5977

Hussain, F., Duraisamy, K.: Mechanics of viscous vortex reconnection. Phys. Fluids (2011). https://doi.org/10.1063/1.3532039

Jaffard, S.: The spectrum of singularities of Riemann's function. Rev. Mat. Iberoam. **12**(2), 441–460 (1996)

Jeong, J., Hussian, F.: On the identification of a vortex. J. Fluid Mech. **285**, 69–94 (1995). https://doi.org/10.1017/S0022112095000462

Jerrard, R.L., Smets, D.: On the motion of a curve by its binormal curvature. J. Eur. Math. Soc. **17**(6), 1487–1515 (2015)

Kida, S., Takaoka, M.: Breakdown of frozen motion of vorticity field and vorticity reconnection. J. Phys. Soc. Jpn. **60**(7), 2184–2196 (1991). https://doi.org/10.1143/JPSJ.60.2184

Kida, S., Takaoka, M., Hussain, F.: Reconnection of two vortex rings. Phys. Fluids A **1**(4), 630–632 (1988)

Klein, R., Majda, A.J.: Self-stretching of a perturbed vortex filament I. The asymptotic equation for deviations from a straight line. Phys. D: Nonlinear Phenom. **49**(3), 323–352 (1991). https://doi.org/10.1016/0167-2789(91)90151-X

Klein, R., Majda, A.J., Damodaran, K.: Simplified equations for the interaction of nearly parallel vortex filaments. J. Fluid Mech. **288**, 201–248 (1995). https://doi.org/10.1017/S0022112095001121

Kumar, S., et al.: The Frisch–Parisi formalism for fluctuations of the Schrödinger equation. arXiv:2202.06645 (2022)

Laporte, F., Leweke, T.: Elliptic instability of counter-rotating vortices: experiment and direct numerical simulation. AIAA J. **40**, 12 (2002)
Le Dizés, S., Lacaze, L.: An asymptotic description of vortex Kelvin modes. J. Fluid Mech. **542**, 69–96 (2005). https://doi.org/10.1017/S0022112005005185
Leweke, T., Le Dizes, S., Williamson, C.H.K.: Dynamics and instabilities of vortex pairs. Annu. Rev. Fluid Mech. **48**, 1–35 (2016). https://doi.org/10.1146/annurev-fluid-000000-000000
Lim, T.T., Nickels, T.B.: Instability and reconnect in the head-on collision of two vortex rings. Nature **357**, 225–227 (1992)
Lipniacki, T.: Quasi-static solutions for quantum vortex motion under the localized induction approximation. J. Fluid Mech. **447**, 321–337 (2003)
McGavin, P., Pontin, D.I.: Vortex line topology during vortex tube reconnection. Phys. Rev. Fluids (2018). https://doi.org/10.1103/PhysRevFluids.3.054701
Melander, M.V., Hussain, F.: Cut-and-connect of two antiparallel vortex tubes. In: Proceedings of the 2nd Summer Program of the Center of Turbulence Research, pp. 257–286. Cent. Turbul. Res., Stanford (1988)
Muzy, J.F., Barcy, E., Arneodo, A.: The multifractal formalism revisited with Wavelets. Int. J. Bifurc. Chaos **4**(2), 245–302 (1993)
Nemirovskii, S.K.: Statistical signature of vortex filaments in classical turbulence: Dog or tail? J. Eng. Thermophys. **29**(1), 14–25 (2020)
Ortega, J.M., Bristol, R.L., Savas, Ö.: Experimental study of the instability of unequal-strength counter-rotating vortex pairs. J. Fluid Mech. **474**, 35–84 (2003). https://doi.org/10.1017/S0022112002002446
Rosenhead, L.: The spread of vorticity in the wake behind a cylinder. Proc. R. Soc. Lond. A **127**, 590–612 (1930). https://doi.org/10.1098/rspa.1930.0078
Schwarz, K.W.: Three-dimensional vortex dynamics in superfluid 4He: line–line and line–boundary interactions. Phys. Rev. B **31**(9), 5782 (1985)
Shaffman, P.G.: Vortex Dynamics. Cambridge University Press, Cambridge (1992)
Turiel, A., Pérez-Vicente, C.J., Grazzini, J.: Numerical methods for the estimation of multifractal singularity spectra on sampled data: a comparative study. J. Comput. Phys. (2006). https://doi.org/10.1016/j.jcp.2005.12.004
Villois, A., Proment, D., Krstulovic, G.: Universal and nonuniversal aspects of vortex reconnections in superfluids. Phys. Rev. Fluids (2017). https://doi.org/10.1103/PhysRevFluids.2.044701
Wendt, H., Abry, P., Jaffard, S.: Bootstrap for empirical multifractal analysis. IEEE Signal Process. Mag. (2007). https://doi.org/10.1109/MSP.2007.4286563
Yao, J., Hussain, F.: A physical model of turbulence cascade via vortex reconnection sequence and avalanche. J. Fluid Mech. (2020). https://doi.org/10.1017/jfm.2019.905
Yao, J., Hussain, F.: Vortex reconnection and turbulence cascade. Annu. Rev. Fluid Mech. **54**, 317–347 (2022). https://doi.org/10.1146/annurev-fluid-030121-125143